SensUs 2026 Parkinson's disease

SensUs

Team Results Document

MakeSense

ShanghaiTech University

TEAM MEMBERS

CAPTAINS

Yangbin Chen
Terry Wang

HARDWARE

Kaizhan Lin
Leyan Cai
Zhiyi Qin
Chuhe Wen

SUPERVISORS

Suwen Zhao
Ze Xiong
Daniel Koo

BIOLOGY

Fusheng Liu
Chaoxin Shan
Zhaoxi Zhang
Yafei Chang
Yuchen Hao
Hongru Tan

TRANSLATION

Runlin Dong
Siyuan Wu
Linjia Liu

上海科技大学
ShanghaiTech University

MakeSense ShanghaiTech



1. Abstract: Summary for the SensUs website

L-DOPA is the gold-standard pharmacotherapy for Parkinson’s disease, but its short half-life leads to concentration fluctuations that are closely associated with motor symptoms. Monitoring L-DOPA could support individualized dosing and assessment of treatment response, yet no suitable clinical tool is available. Therefore, we developed a wearable electrochemical L-DOPA sensor that integrates an enzyme-functionalized, L-DOPA-selective microneedle with low-noise electronics to enable continuous monitoring of L-DOPA in interstitial fluid (ISF).

The system incorporates advances in both molecular recognition and electronic readout. We used polyphenol oxidase (PPO) as the biorecognition element. However, its cross-reactivity with physiological tyrosine causes major interference and limits detection specificity. Starting from the native dicopper pocket of a PPO, we performed de novo protein design and obtained proteins that retained catalytic activity toward L-DOPA but showed no detectable activity toward tyrosine. For readout, we developed a coin-sized electrochemical platform for wearable measurement of picoampere-scale sensor currents.

During in vivo evaluation, the integrated microneedle system recorded continuous signals following L-DOPA administration, supporting the feasibility of continuous monitoring. Overall, this work provides a new tool for tracking L-DOPA exposure and a general route for applying de novo-designed catalytic proteins in biosensing.

2. AP award: Biosensor developed for the Eindhoven Testing Event

2.1. Molecular recognition

Polyphenol oxidase (PPO) is used as the molecular recognition element to oxidize L-DOPA to electrochemically reducible dopaquinone. The PPO can be either commercially available mushroom tyrosinase or a de novo-designed protein (Figure 1A).

For sensor fabrication, PPO is mixed with trehalose, Triton X-100, and bovine serum albumin, cross-linked with glutaraldehyde, and drop-cast onto the working electrode (Brunetti et al., 2014). After drying, a waterborne polyurethane outer membrane is applied to form an enzyme-immobilized multilayer biorecognition interface (Figure 1B). During Days 2-5 of storage in PBS, the sensor retained linear calibration responses, with sensitivity bias and baseline deviation within ±13% (Figure 1C).

2.2. Physical transduction

L-DOPA is oxidized by PPO to dopaquinone, which can be electrochemically reduced at −0.2 V versus Ag/AgCl, a potential at which responses from common electroactive interferents are low (Tesoro et al., 2023). We therefore used chronoamperometry at −0.2 V to measure the cathodic current generated by the reduction of dopaquinone back to L-DOPA (Figure 1A). The calibration was linear over 3-50 µM L-DOPA (R^2 = 0.99962; Figure 1D).

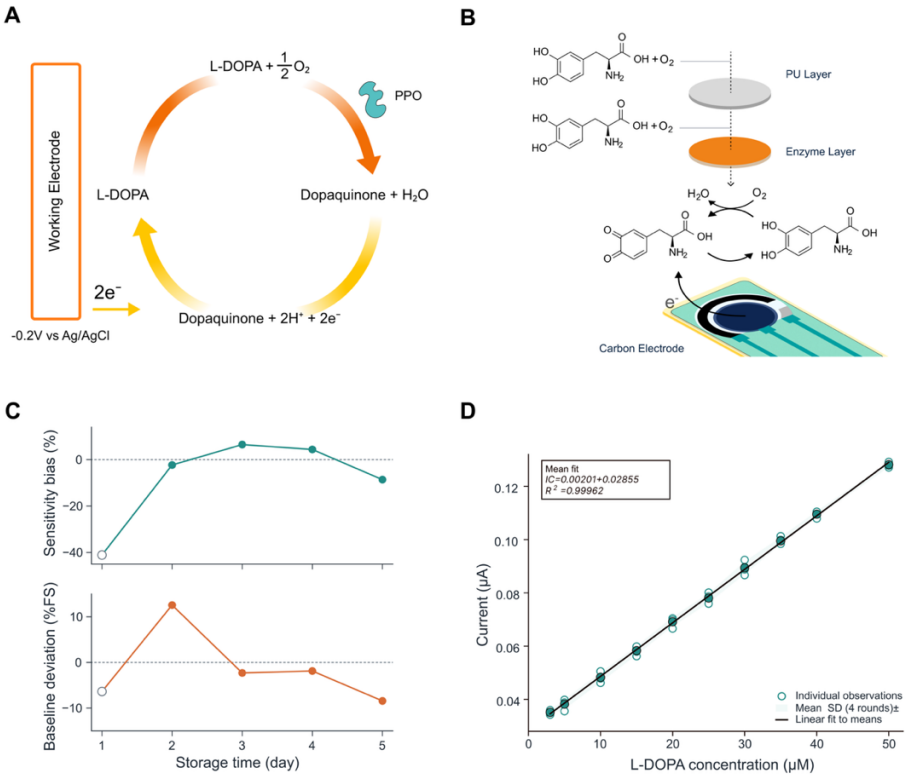


Figure 1. L-DOPA biosensor construction and analytical performance. (A) Detection principle. (B) Sensor architecture. (C) Sensitivity and baseline changes during storage in PBS. (D) Calibration in PBS.

2.3. Cartridge technology

The microfluidic cartridge was designed to integrate a screen-printed electrode without permanent bonding to the electrode surface. A pre-cured PDMS spacer containing a 10 mm circular opening was aligned with the sensing area to form a chamber volume of approximately 50 µL. The electrode and spacer were enclosed between upper and lower PDMS support layers and compressed by two rigid polymer plates using torque-controlled threaded fasteners. This mechanically assembled structure improved sealing, maintained a reproducible chamber geometry, and allowed convenient electrode replacement. The chamber-facing PDMS surfaces were hydrophilically treated to promote uniform wetting and reduce bubble entrapment. For sample delivery, a 150 µL reservoir with an upper-wide and lower-narrow geometry was connected to the chamber through polyethylene tubing. A microinjection pump withdrew liquid from the outlet at 100 µL/min, generating negative pressure for controlled sample introduction and replacement.

2.4. Reader instrument and user interaction

Recording that reduction current on the body, rather than at a bench, is what the reader has to do: hold the working electrode at the set potential, resolve a picoampere-level current and deliver the result unattended, all from a coin cell. Its electrical configuration and measured performance are given in the Appendix.

Hardware

The unit is a two-layer board, 27.20 × 20.04 mm (386 mm^2), carrying two active devices: a MAX30131 integrated electrochemical front end in a 2.93 × 2.93 mm wafer-level package, which places the potentiostat, a 16-bit current ADC and two setpoint DACs on one die, and an nRF52833 Bluetooth Low Energy controller. A CR2032 coin cell supplies both directly, so the unit contains no power-management integrated circuits. The cell holder occupies 49 % of the board and the two circuits together 34 mm^2:

Software

The firmware configures the front end, verifies every setting by reading it back and then lets it convert autonomously; brown-out detection and a watchdog must arm before acquisition starts. Gain is calibrated once against the factory-trimmed range and stored, so the user performs no calibration at the time of use.

User handling and interface

The wearer is not tethered. The user connects the electrode array and inserts the coin cell; the unit then advertises over Bluetooth Low Energy and pushes each result as its

conversion completes, so the operator watches a live trace rather than requesting data. Potential, current range and duration are set from the host, so a measurement can be reconfigured without reprogramming the unit. The 256-sample on-chip buffer covers a brief loss of radio contact without leaving a gap, and every result carries a sequence number and validity flags so that loss is reported rather than interpolated over.

3. IN award: Biosensor innovation

To address the need for continuous L-DOPA monitoring, we developed an L-DOPA sensor that enables wearable monitoring with reliable signal output. To realize wearable operation, we integrated coin-sized hardware for picoampere electrochemical readout with an enzyme-modified microneedle, which generated continuous in vivo signals in an animal model. To improve reliability, we developed a de novo-designed enzyme that eliminated the principal interference. The resulting system provides a feasible approach for monitoring L-DOPA concentrations in interstitial fluid.

3.1. Wearable sensor

The wearable system comprises a flexible three-electrode microneedle and a coin-sized electrochemical front end. Polyphenol oxidase (PPO) immobilized on the microneedle working electrode oxidizes L-DOPA in interstitial fluid to dopaquinone. At an applied negative potential, dopaquinone is reduced at the working electrode, generating a picoampere-level reduction current that is measured by the electrochemical front end.

3.1.1. Technological novelty of wearable sensor

The sensor employs a flexible three-electrode microneedle, with the working, reference, and counter electrodes integrated on a single flexible substrate and an insertion depth of approximately 5 mm. A cross-linked enzyme layer is formed on the working electrode, while the entire microneedle electrode is covered by a waterborne polyurethane outer membrane, creating a localized electrochemical biosensing interface with subcutaneous interstitial fluid after insertion (Figure 2A).

The low-current signal generated by the microneedle requires a readout system that combines potentiostatic control, picoampere-level measurement, wireless communication, low power consumption, and miniaturization. We therefore developed coin-sized wearable electrochemical hardware integrating potentiostatic control, current acquisition, analog-to-digital conversion, wireless communication, and battery power on a single platform. The final device comprises two integrated circuits and 27 components on a two-layer, 386 mm^2 circuit board powered directly by a coin-cell battery (Figure 2B).

The analog front end was designed using the measured impedance and noise characteristics of the sensing electrode rather than generic parameters such as amplifier input bias current alone. Compared with the previous discrete architecture, which comprised 10 integrated circuits, 112 components, a six-layer circuit board, and two stacked boards, the final design replaces multiple independent analog modules with an integrated

electrochemical front end. It retains potentiostatic control and low-current readout while substantially reducing component count, layer count, and board area, enabling picoampere electrochemical measurement in a coin-cell-powered wearable platform.

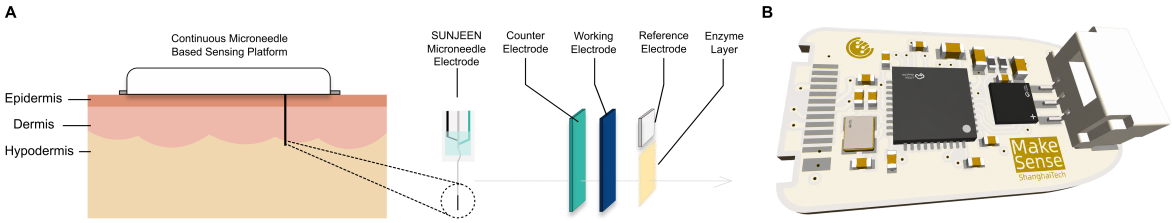


Figure 2. Wearable L-DOPA sensing system. (A) Flexible three-electrode microneedle. (B) Coin-sized electrochemical readout hardware.

3.1.2. Technical feasibility of wearable sensor

In PBS, the enzyme-modified microneedle responded linearly to 0.156-10 μM L-DOPA, with a sensitivity of 0.226 nA/μM and an R^2 of 0.998 (Figure 3A). At the lowest tested concentration, the corresponding current increment was approximately 35 pA, placing the analytically useful signal directly within the picoampere range.

The readout resolves that increment with margin. Table 1 gives the measured performance of the wearable front end. On its lowest full-scale range the quantisation step is 0.763 pA and the measured noise is 1.71 pA rms, so the 35 pA increment corresponding to the lowest calibrated concentration is 6.9 times the instrument's three-standard-deviation figure, and 12.4 times it after the 19 s averaging at which the Allan deviation reaches its minimum. The same measured impedance spectrum that was used to specify the front end also fixes the electrode's own thermal-noise floor, which is 0.18 pA at three standard deviations: the instrument sits about thirty times above that bound, so the limit on resolution lies in the electronics and not in the electrode, and the remaining margin is available to further design rather than being thermodynamically closed.

Parameter	Value	Condition
Quantisation step	0.763 pA	50 nA full scale, 16-bit conversion
Noise, 1 SD	1.71 pA	Electrode port open; 1.88 s integration; 5.5 min record
Noise, 3 SD	5.12 pA	As above
Noise-free resolution	12.7 bit	As above
Minimum Allan deviation	0.945 pA at 18.8 s	As above
Electrode thermal-noise floor, 3 SD	0.18 pA	From the measured impedance spectrum; contains no instrument parameter
Smallest calibrated signal increment	35 pA	0.156 μM step at 0.226 nA/μM
Margin of that increment over 3 SD	6.9× (12.4× at 18.8 s)	Ratio of the two rows above

Table 1. Measured performance of the wearable electrochemical front end.
Hardware data-sheet reference: Analog Devices (2026).

Noise on a connected electrode is larger than the open-port figure, because the amplifier's voltage noise then develops across the electrode impedance; that contribution is configuration-dependent and is reported in the Appendix together with the conditions under which it was measured.

To evaluate in vivo feasibility, we implanted the enzyme-modified microneedle subcutaneously in a rat model and administered L-DOPA intraperitoneally. The sensor recorded a continuous, time-dependent electrochemical response over 1 h, with readouts obtained at approximately 3-min intervals (Figure 3B).

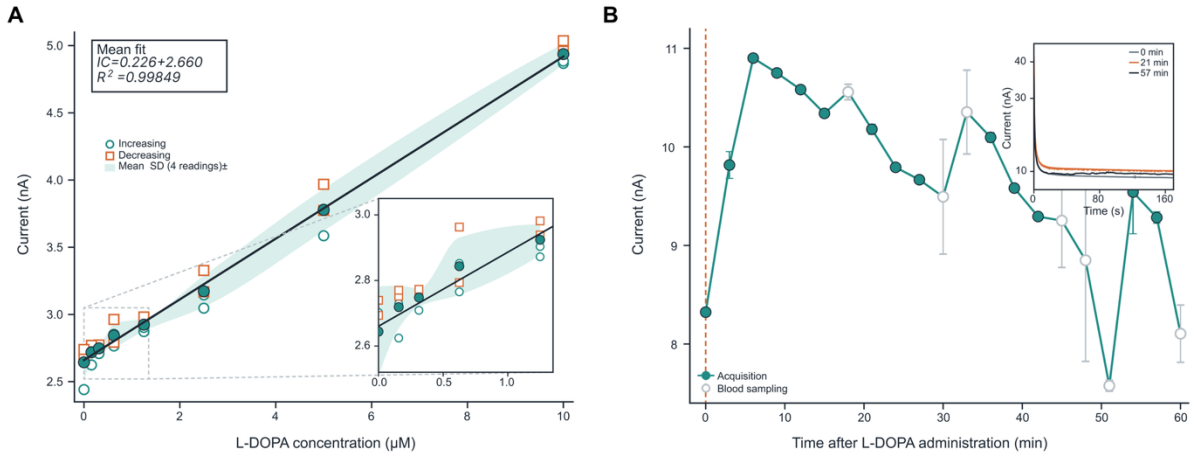


Figure 3. Wearable-sensor feasibility. (A) Microneedle calibration in PBS. (B) Continuous in vivo response after L-DOPA administration.

The present work demonstrates a linear in vitro response and continuous in vivo signal acquisition, supporting the feasibility of our L-DOPA monitoring system. Future work will focus on further integrating the system, evaluating it in larger animal cohorts, and expanding in vivo testing.

3.2. Reliability of sensor output

The preceding circuit and microneedle designs reduced device-related errors and enabled wearable picoampere-level current detection. Reliability also requires selective recognition of L-DOPA. Tyrosinase is used in electrochemical L-DOPA biosensors (Brunetti et al., 2014; Tesoro et al., 2023), but it oxidizes both L-DOPA and L-tyrosine (Fernandez-Julia et al., 2021). In our interference assessment, tyrosine was the only tested compound expected to produce physiologically significant interference. Because circulating tyrosine varies with circadian rhythm and nutritional intake (Melamed et al., 1980; Wurtman et al., 1967), this cross-response could be misinterpreted as an in vivo L-DOPA fluctuation. We therefore require an enzyme that catalyzes diphenols but not monophenols.

3.2.1. Technological novelty of reliability concept

We initially searched for natural PPOs with the required selectivity, but most candidates were plant-derived and difficult to express and purify in prokaryotic systems (Dirks-Hofmeister et al., 2013). Moreover, no validated method can predict their tyrosine monophenolase activity (Prexler et al., 2019). These limitations made natural-enzyme mining inefficient. Considering that biosensing requires only sufficient activity to generate a readable electrochemical signal and places greater emphasis on selectivity and stability than on maximal turnover, we adopted de novo protein design to generate candidate proteins for L-DOPA sensing.

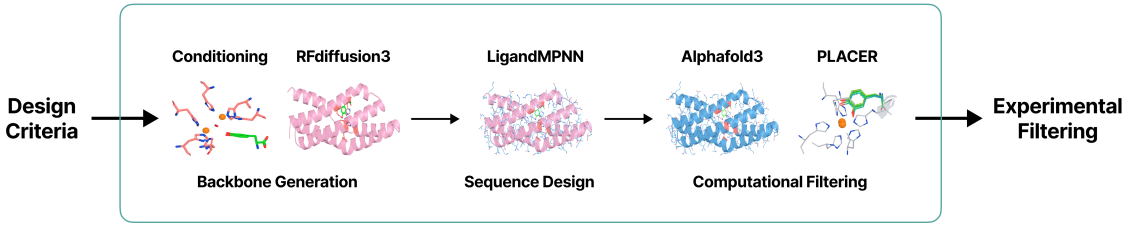


Figure 4. De novo design and experimental screening workflow.

We selected the Bacillus megaterium tyrosinase TyrBm (UniProt B2ZB02, PDB 4P6S) as the natural PPO reference (Goldfeder et al., 2014) and used AlphaFold 3 to co-fold it with all active-site ligands and cofactors (Abramson et al., 2024). From the resulting model, we extracted six copper-coordinating histidines, two Cu ions, a bridging peroxide, and L-DOPA as the theozyme. We then used RFdiffusion3 to generate protein backbones around this fixed motif and LigandMPNN to design sequences in the metal- and ligand-containing context (Butcher et al., 2025; Dauparas et al., 2025). Finally, we used AlphaFold 3 and PLACER to screen the resulting designs based on the overall fold, local metal coordination, and ligand pose (Abramson et al., 2024; Anishchenko et al., 2025). Designs passing the computational filters were advanced to wet-lab evaluation.

3.2.2. Technical feasibility of reliability concept

Following three rounds of design and structural screening around the transplanted functional pocket, 33 proteins were selected for wet-lab evaluation. Expression and functional screening have currently been completed for 12 candidates, among which Designs 15 and 17 exhibited detectable L-DOPA oxidation activity.

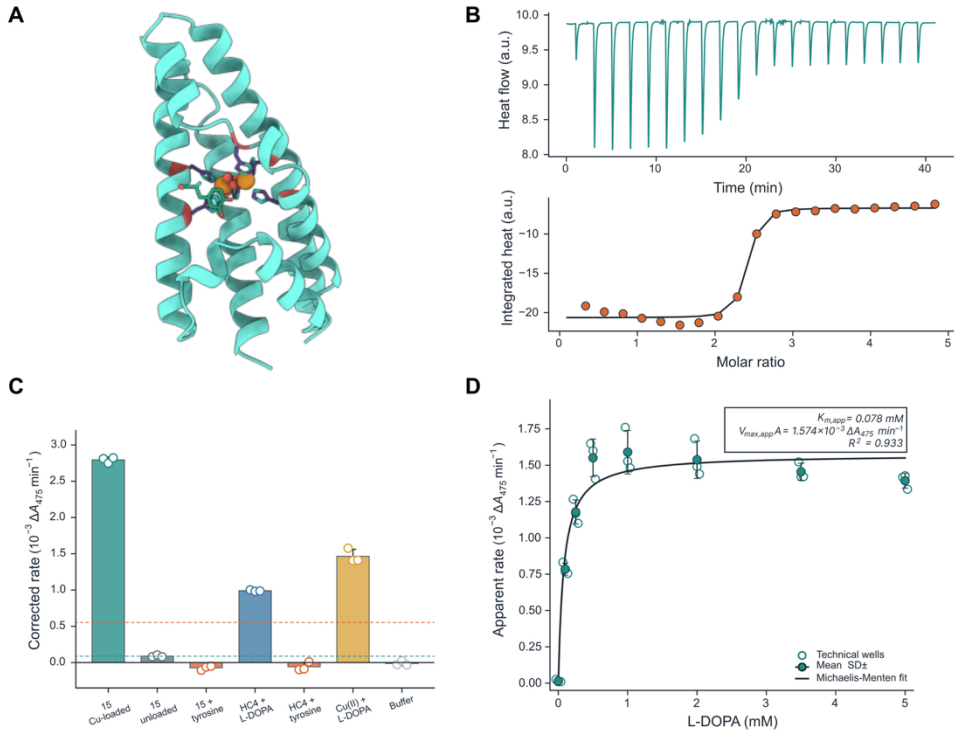


Figure 5. Evaluation of Design 15. (A) Predicted complex. (B) Cu(II)-binding ITC. (C) L-DOPA activity and controls. (D) Apparent kinetics.

After Cu(II) loading and buffer exchange, the background-subtracted apparent rate of increase in A475 for loaded Design 15 was 2.79 ± 0.04 × 10^{-3} ΔA475 min^{-1} at 1 mM L-DOPA and 0.3 mg mL^{-1} protein (mean ± SD, n = 3 technical replicates; Figure 5C). The loaded sample exceeded unloaded Design 15, the non-copper-binding protein, and buffer. Free Cu(II) produced a lower signal and therefore did not account for the full Design 15 response. HC4, a reported de novo dicopper catechol oxidase, served as the positive control (Eng et al., 2026). Under the same substrate-testing conditions, Design 15 responded to L-DOPA, whereas its tyrosine response did not exceed the corresponding background threshold.

ITC analysis of Cu(II) binding to Design 15 yielded an apparent dissociation constant (Kd) in the nanomolar range, a binding stoichiometry N = 2.30 ± 0.02, and an enthalpy change ΔH = −14.0 ± 0.3 kcal mol^{-1} (Figure 5B). L-DOPA concentration-dependent initial rates yielded an apparent Michaelis constant Km,app = 0.078 mM and an apparent maximum rate Vmax,app = 1.574 × 10^{-3} ΔA475 min^{-1} (Figure 5D). Together, these results demonstrate Cu(II)-dependent L-DOPA oxidation by Design 15 without a detectable tyrosine monophenol response. No catalytic response has been detected after electrode immobilization so far.

The present work demonstrates that de novo protein design can generate a copper-dependent L-DOPA-oxidizing protein without detectable activity toward tyrosine, supporting its feasibility for improving molecular selectivity in biosensing. The cause of the absent response after electrode immobilization remains unresolved. Future work will focus

on improving enzyme activity and stability and optimizing the immobilization process, with the goal of achieving a measurable catalytic response on the electrode.

3.3. Original contributions

Team Statement

We selected PPO-based electrochemical detection as the core strategy for L-DOPA sensing and developed the wearable system around this principle.

For the sensing interface, we developed an enzyme-functionalized three-electrode microneedle with a cross-linked protein layer and a waterborne polyurethane outer membrane. After identifying tyrosine cross-reactivity as the principal molecular interference, we developed a de novo protein design strategy based on a natural dicopper pocket and obtained candidate proteins with L-DOPA activity but no detectable tyrosine activity.

We also developed a coin-sized wearable electrochemical platform capable of picoampere-level current measurement and integrated it with the microneedle sensor. The microneedle produced linear responses in vitro and continuous electrochemical signals in an animal model.

Project conception, route selection, technical development, experimentation, iteration, and data analysis were completed independently by the student team. External support was limited to published literature, open-source tools, shared research facilities, resource provision, and overall academic supervision.

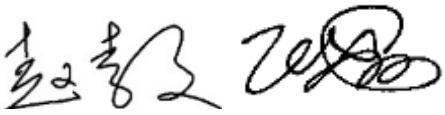
Supervisor Statement

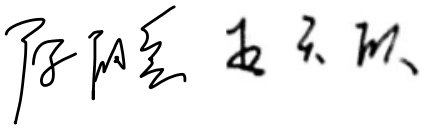
The student team demonstrated strong independent research capabilities in developing the wearable L-DOPA monitoring system. The supervisor’s role was limited to providing research resources and experimental conditions, conducting overall academic supervision, and evaluating project progress.

The team independently evaluated different sensing strategies, selected the PPO-based electrochemical route, and identified tyrosine cross-reactivity as the principal molecular interference. The students subsequently developed the de novo protein design strategy and completed the associated computational and experimental validation.

The team autonomously completed microneedle functionalization, circuit development, system integration, electrochemical characterization, computational protein design, protein production and biochemical testing, animal experiments, and data analysis. The supervisor monitored scientific rigor, research conduct, safety, and ethical compliance without replacing the students in technical development, experimentation, or decision-making.

The resulting work reflects the student team’s independence in scientific conception, technical implementation, experimental validation, and interpretation, as well as its capacity for rigorous and original research.





3.4. Bonus criteria Innovation

Enzyme-based electrochemical sensing depends on a suitable oxidoreductase and is therefore limited to a relatively small subset of analytes. Binding-based recognition does not require chemical conversion and can be applied more broadly, including to small molecules (Benson et al., 2001; Kang et al., 2017). Solute-binding proteins (SBPs) bind small-molecule ligands and undergo ligand-induced conformational changes. We therefore sought to construct a platform that converts this allosteric signal into a readable electrochemical output.

We designed a platform that directionally anchors an SBP to the electrode and attaches a redox reporter to the protein. The conformational change alters the reporter-to-electrode distance and electron transfer (Figure 6C; Benson et al., 2001). In parallel, we redesigned SBPs for L-DOPA recognition and evaluated binding using differential scanning fluorimetry (DSF). No designed candidate showed detectable L-DOPA binding, whereas the 3LFT–tryptophan pair served as the positive control (Figure 6A). Successful SBP modification and electrode coupling were confirmed. Ligand addition produced an electrochemical response, but the signal did not recover as the ligand concentration decreased. The cause of this irreversible behavior has not yet been identified (Figure 6B).

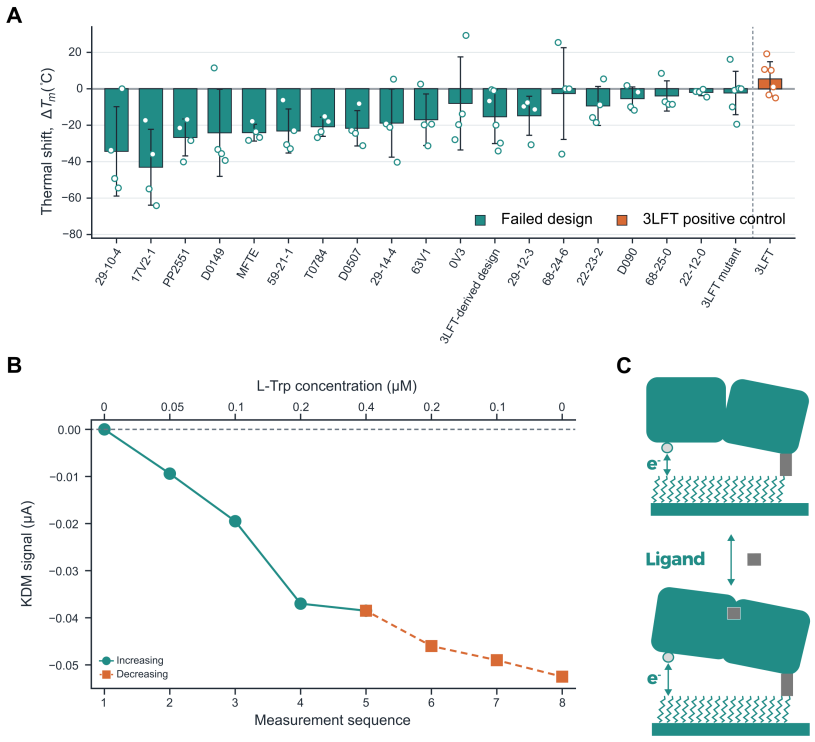


Figure 6. SBP-based electrochemical sensing platform. (A) DSF screening of designed L-DOPA-binding SBPs, with the 3LFT–tryptophan pair as the positive control. (B) Electrochemical responses during increasing and decreasing ligand concentrations. (C) Conformation-dependent electrochemical transduction principle.

Although a functional L-DOPA-specific SBP sensor has not yet been achieved, this binding-based platform remains worth pursuing. Future work will focus on obtaining effective L-DOPA-binding SBPs, identifying the source of signal irreversibility, and optimizing electrochemical coupling to achieve reversible transduction.

4. TP award: Translation potential

4.1. Customer interviews

4.1.1. Identification of potential stakeholders

Levodopa dosing is not decided by one person: the schedule is set, contested and revised by the patient, the family member who manages the medication, the neurologist who owns the decision, and the clinician-scientist who defines what counts as evidence. We sampled all four through a clinical referral chain; caregivers matter because in 11/20 (55%) the patient was not the main speaker (Table 2).

Table 2. Stakeholders engaged, November 2025 – July 2026; clinic observation in §4.1.2.

Group	Who	Why relevant
Neurologists (5; HP1–HP5)	Tertiary movement-disorder specialists; one runs pre-DBS titration, one has ~10 000 consultations	The only people who can act on an exposure curve
Patients, in-home (3)	P1 F, PD ≈ 6.5 y, retired surgeon; P2 M, 75 y, PD ≈ 16 y, self-optimiser; P3 M, 68 y, mild, opposed	Spread across health literacy, disease duration, attitude
Patients / caregivers (≈ 6)	One patient of 8 years had stopped medication entirely	Absent from any compliant cohort

Declaration of interest. HP3 has been our advisor since April 2026; his input is substantive but not arm's-length, so he is excluded from the L4 analysis and serves as its pilot (A3). *Limitation.* Three in-depth patient interviews is below the five-per-segment rule of thumb and we interviewed no GP or nurse — a gap, though titration sits in tertiary clinics.

4.1.2. Interview approach and execution

Four complementary methods. *Narrative interviews at home* (3 patients, 40-60 min) turned on one question — "walk me through yesterday, from the moment you woke up" — with a 17-item probe guide never read out, asking only about concrete past events (Fitzpatrick, 2013); *contextual inquiry* recorded the home environment as data. *Clinician interviews* (5, 30-60 min) covered titration practice, missing information and interpretability. *Clinic observation* timed 20 consecutive consultations, separating observed from inferred. Preparation and ethics. A clinician reviewed the protocol in writing beforehand, and his questions produced the segmentation in Table 2. We never introduced the product concept and never commented on a patient's self-adjustment — we recorded it, we did not judge it. Recording followed verbal consent, the clinic saw no capture of any kind, and identifiers were removed before analysis (A2).

4.1.3. Interview results and conclusions

1 — What is adjusted is the schedule, and patients adjust it too. Medication changed on the spot in 15/20 consultations, at a median 13 minutes (5-26, n = 19), and 13/20 (65%) brought a handwritten record. The smallest usable division is a quarter tablet, so fine titration by amount is impossible. Patients act on the same variable: P1 moved her first dose to 05:00-05:30 and proposed a reduction herself; P2 split his controlled-release tablet — "by two o'clock there was no drug left. So I — on my own initiative — telephoned my doctor." In two of three cases the therapeutic idea came from the patient, and 7/20 (35%) had adjusted or wanted to; what stops the rest is the absence of a signal (A1).

2 — Clinicians converge on within-patient shape and on attribution, not advice. HP1 named the absence of *in-situ, dynamic measurement*; HP4, that change matters more than an accurate number; HP5 asked *how would you calibrate that?* Independently, three months earlier, HP3 wrote that it "may only work… as individualised, longitudinal within-patient monitoring", then defined the product: "Your job at the start should not be to tell the physician what to decide, but to help the physician work out why." HP3 shaped the study, so this is advisory input, not confirmation.

Conclusion — the problem to be solved. Patients report events where physicians need a curve, and absorption — a determinant of the on–off phenomenon (Nutt et al., 1984) — is measured nowhere in the care we observed (A1); both point at peripheral exposure. Neither can distinguish three situations behind one complaint — absorbed but run out, absorbed late, never absorbed — which need opposite actions. What is needed is an objective description of each patient's own exposure over time.

4.2. Design of validation study

4.2.1. Selection of the problem

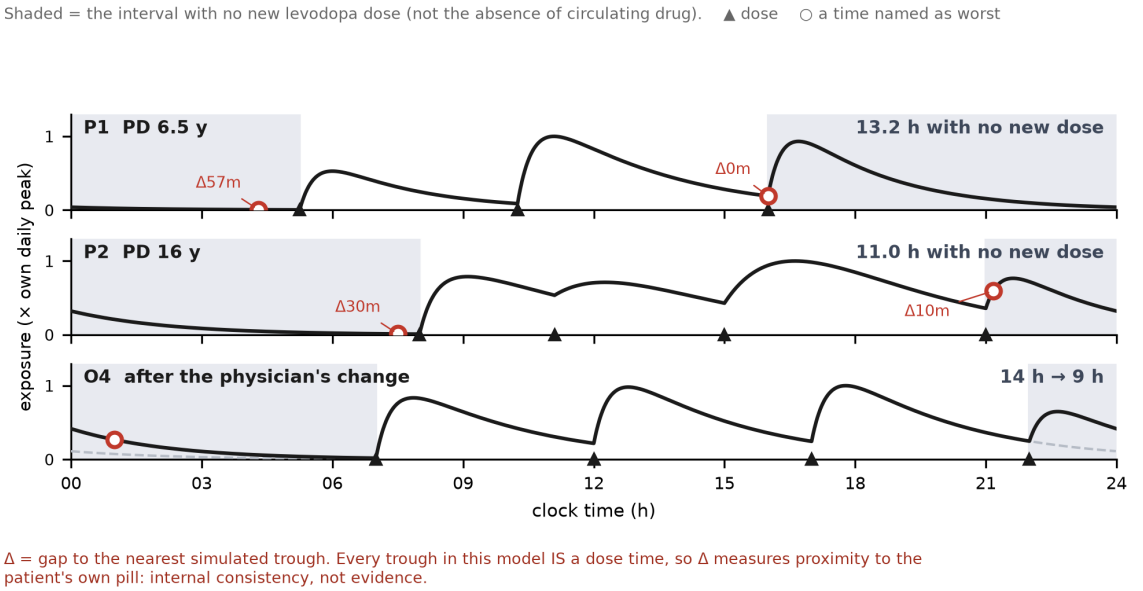


Figure 7. Simulated L-DOPA exposure from reported dosing schedules (one-compartment model, uncalibrated).

One segment of the day is invisible to every method. By arithmetic, 13.2 h pass for P1 and 11.0 h for P2 between their last evening and first morning doses, at about 22% of their own daily peak on average. Nothing reports on it: the patient sleeps, motion sensing cannot tell if immobility is pharmacokinetic, home sampling is infeasible, the diary blank.

Problem statement. A third patient (O4) woke at 01:00 unable to turn over; half a tablet at bedtime shortens his interval from ~14 h to 9 h in our model, while the night's deepest point stays immediately before the next morning's dose — the physician treated the complaint he heard and could not check. Neither side can observe exposure across that 11.0-13.2 h interval, in a disease affecting ≥ 4.12 million people in China (Wang et al., 2025).

4.2.2. Conceptual design and use case

Concept. Continuous levodopa monitoring is the missing measurement in Parkinson's pharmacotherapy (Probst et al., 2024). We propose a skin-worn microneedle sensor measuring levodopa in interstitial fluid overnight for 12-14 h (§4.2.1) not for weeks, cutting the in-wear stability requirement to hours (§4.3). Its output is a shape, not a number: whether a dose reached the person's own peak (S2) and how long it held (S3) — the two problems our advisor named unprompted — plus onset and the nadir's depth and clock time (A8).

Calibration and use. Not against a population: three enrolment nights on the unchanged regimen, aligned with that patient's own symptom events, give two thresholds belonging

to them alone (A7). We claim no comparability between patients, and it recommends no dose: following HP3's "there is no fixed rule", it classifies the exposure problem. The patient wears the sensor for three nights between visits and brings back one A4 sheet, readable in under 90 s against a 13-minute consultation.

Feasibility and novelty. The microneedle format is established in continuous glucose monitoring; the novel elements are §3's picoampere readout and *de novo* recognition element, and this output layer. That element makes overnight use possible: natural tyrosinase cannot separate levodopa from tyrosine, which has a daily rhythm (Wurtman et al., 1967).

4.2.3. Validation study design

We lack one measurement capability, but testing a causal chain needs less: each link is validated with a method that exists now, and what would refute us is fixed in advance.

Table 3. Validation ladder; refutation criteria fixed before data collection (L4 protocol: A3).

	What it tests, and the method available today	**Refuted if**
L1	the model behind Figure 7 — drive it with published plasma levodopa profiles and compare point by point	the tail criterion fails → the Figure 7 overnight figures are withdrawn
L2	whether pre-dawn exposure is as low as predicted — a ratio, not a curve: two carer-collected dried blood spots per patient, pre-dawn and near peak, 6-10 patients (A5)	ratio > 0.4 in half or more patients → the overnight-vacuum framing is wrong
L3	whether exposure change is associated with nocturnal symptoms — natural experiment on bedtime-dose changes made anyway; symptom scale plus accelerometer turning counts, 5-7 nights each side	improvement even across the night, or before dawn → the nadir-clock parameter is rebuilt
L4	whether the curve changes the decision and whether it misleads — within-clinician, counterbalanced, cause-blinded vignette study: 8 seeded vignettes (three causes) and 2 decoys (A3)	no better than chance → revise the display; reading > 90 s → not viable; decoy over-attribution → a harm signal

L1 establishes model validity, not clinical validity. L4 is a pilot, not powered for hypothesis testing, whose decoy arm is a safety endpoint.

4.3. Bonus criteria Translation Potential

A regulatory strategy built as a ladder of claims. Rather than one intended use we specified five claim levels, from research-use instrument to a product whose output enters a treatment decision, separating the evidence line (what must be shown) from the registration line (what must be filed, and when). That stops scope expanding silently with each new result; a design-freeze gate fixes the point after which any change to the recognition layer forces revalidation. §4.2.2 sits low on this ladder: the commercially attractive claim and the defensible claim are not the same, and we chose the defensible one.

Sterilisation and storage: a failure mode named early. Three risks remain: enzyme activity after terminal sterilisation, shelf-life stability of the electrode, and stability during wear. Sterilisation compatibility has no known route and surfaces only once the rest is ready. One-night wear reduces only the third — one risk down, not readiness.

A cost ceiling set by what the therapy itself costs. Our advisor corrected an over-estimate: levodopa costs 60-70 RMB a pack, under 150 RMB a month for many patients, while one inpatient episode is an order of magnitude higher (mean 11,463.57 RMB; Wang et al., 2025). A product optimising a therapy costing under 150 RMB a month cannot be priced as though it were the therapy — hence a low-cost disposable used episodically, three nights between visits. They constrain price; they do not establish willingness to pay.

A reusable field instrument, and an honest report of how it failed. Our 20-column observation sheet collapsed under time pressure — the tick-box columns were left almost entirely empty, while the free text produced essentially everything in §4.1.3: a structured instrument competes for the observer's attention with the thing observed. The revision is free text plus three counters (A6). Two gaps followed — no data on willingness to pay or travel burden — so any pricing claim is unfounded.

5. Team and support

5.1. Contributions of the team members

(Listed in no particular order)

Yangbin Chen: Team captain, hardware development

Terry Wang: Team captain, management, sensor system overall design, de novo protein design, wet-lab experiments

Kaizhan Lin: Hardware leader

Runlin Dong: Commercialization, design

Fusheng Liu: Protein design, microneedles, animal experiments, MLDE method development, wet-lab experiments

Yuchen Hao: Wet-lab experiments

Yafei Chang: SBP technical approach, wet-lab experiments

Chaoxin Shan: Wet-lab experiments

Zhaoxi Zhang: Electrochemistry technical approach, wet-lab experiments

Leyan Cai: Hardware development

Hongru Tan: Wet-lab experiments

Siyuan Wu: Commercialization, Design

Zhiyi Qin: Hardware development

Chuhe Wen: Microfluidics development

Linjia Liu: Software development

5.2. People who have given support

Dr. Yiqi Liu, a physician-scientist specializing in neurology at the Shanghai Clinical Research and Trial Center, has provided ongoing consultation on the clinical framework and academic research value of levodopa, as well as practical guidance on its implementation.

Mr. Jifei Yang, of Sanjun Electrochemistry provided technical support for electrode development.

Junfeng Wang, of the Animal Core Facility, ShanghaiTech University, assisted in conducting the animal experiments.

Xiuxia Gao performed protein-protein interaction characterization.

Jing Yang was responsible for consumables procurement and laboratory management.

5.3. Sponsors and partners

Demcon, Panton, BOM, Philips:

Conducted the Partner Session with us and provided guidance on the technical solution and commercialization of sensors.

6. Final remarks

For our team, the SensUs Competition is not the end of the project, but a milestone in its continued development. To carry it forward, we have established a company, begun formal fundraising efforts, and started working with industry experts. These steps mark the beginning of our efforts to translate the biosensor from a research project into a product with real-world impact.

Following the Competition, we will continue to validate and refine the technology, advance product development, and explore potential clinical and commercial pathways. Building on the progress made through SensUs, we hope to develop a practical solution that delivers meaningful value to patients and healthcare professionals.

We would like to express our sincere gratitude to the School of Life Science and Technology, the School of Biomedical Engineering, the School of Physical Science and Technology, and the School of Creativity and Art at ShanghaiTech University for their generous support. We are also deeply grateful to everyone who has supported us along the way and helped make this journey possible.

7. References

Abramson, J., Adler, J., Dunger, J., Evans, R., Green, T., Pritzel, A., Ronneberger, O., Willmore, L., Ballard, A. J., Bambrick, J., Bodenstein, S. W., Evans, D. A., Hung, C.-C., O'Neill, M., Reiman, D., Tunyasuvunakool, K., Wu, Z., Žemgulytė, A., Arvaniti, E., … Jumper, J. M. (2024). Accurate structure prediction of biomolecular interactions with AlphaFold 3. *Nature, 630*(8016), 493-500. https://doi.org/10.1038/s41586-024-07487-w

Analog Devices. (2026). *MAX30131/MAX30132/MAX30134: 1-, 2-, 4-channel, ultra-low power electrochemical sensor AFEs (Rev. 5)* [Data sheet]. https://www.analog.com/media/en/technical-documentation/data-sheets/max30131-max30132-max30134.pdf

Anishchenko, I., Kipnis, Y., Kalvet, I., Zhou, G., Krishna, R., Pellock, S. J., Lauko, A., Lee, G. R., An, L., Dauparas, J., DiMaio, F., & Baker, D. (2025). Modeling protein–small molecule conformational ensembles with PLACER. *Proceedings of the National Academy of Sciences, 122*(45), e2427161122. https://doi.org/10.1073/pnas.2427161122

Arroyo-Currás, N., Somerson, J., Vieira, P. A., Ploense, K. L., Kippin, T. E., & Plaxco, K. W. (2017). Real-time measurement of small molecules directly in awake, ambulatory animals. *Proceedings of the National Academy of Sciences of the United States of America, 114*(4), 645-650. https://doi.org/10.1073/pnas.1613458114

Benson, D. E., Conrad, D. W., de Lorimier, R. M., Trammell, S. A., & Hellinga, H. W. (2001). Design of bioelectronic interfaces by exploiting hinge-bending motions in proteins. *Science, 293*(5535), 1641-1644. https://doi.org/10.1126/science.1062461

Broothaerts, W., McPherson, J., Li, B., Randall, E., Lane, W. D., & Wiersma, P. A. (2000). Fast apple (Malus × domestica) and tobacco (Nicotiana tobacum) leaf polyphenol oxidase activity assay for screening transgenic plants. *Journal of Agricultural and Food Chemistry, 48*(12), 5924-5928. https://doi.org/10.1021/jf000599m

Brunetti, B., Valdés-Ramírez, G., Litvan, I., & Wang, J. (2014). A disposable electrochemical biosensor for L-DOPA determination in undiluted human serum. *Electrochemistry Communications, 48*, 28-31. https://doi.org/10.1016/j.elecom.2014.08.007

Butcher, J., Krishna, R., Mitra, R., Brent, R. I., Li, Y., Corley, N., Kim, P. T., Funk, J., Mathis, S., Salike, S., Muraishi, A., Eisenach, H. E., Thompson, T. R., Chen, J., Politanska, Y., Sehgal, E., Coventry, B., Zhang, O., Qiang, B., … Baker, D. (2025). *De novo design of all-atom biomolecular interactions with RFdiffusion3* [Preprint]. bioRxiv. https://doi.org/10.1101/2025.09.18.676967

Dauparas, J., Lee, G. R., Pecoraro, R., An, L., Anishchenko, I., Glasscock, C., & Baker, D. (2025). Atomic context-conditioned protein sequence design using LigandMPNN. *Nature Methods, 22*(4), 717-723. https://doi.org/10.1038/s41592-025-02626-1

Derardja, A. E., Pretzler, M., Kampatsikas, I., Barkat, M., & Rompel, A. (2017). Purification and characterization of latent polyphenol oxidase from apricot (Prunus armeniaca L.). *Journal of Agricultural and Food Chemistry, 65*(37), 8203-8212. https://doi.org/10.1021/acs.jafc.7b03210

Dirks-Hofmeister, M. E., Kolkenbrock, S., & Moerschbacher, B. M. (2013). Parameters that enhance the bacterial expression of active plant polyphenol oxidases. *PLOS ONE, 8*(10), e77291. https://doi.org/10.1371/journal.pone.0077291

Eng, V. H., Narehood, S. M., Li, Y., Gascón, M., Hoffnagle, A. M., Shiau, A. A., Semonis, M., Green, M. T., Britt, R. D., & Tezcan, F. A. (2026). Computational design of a highly stable dicopper catechol oxidase. *Journal of the American Chemical Society, 148*(8), 8361-8373. https://doi.org/10.1021/jacs.5c18979

Fernandez-Julia, P. J., Tudela-Serrano, J., Garcia-Molina, F., Garcia-Canovas, F., Garcia-Jimenez, A., & Munoz-Munoz, J. L. (2021). Study of tyrosine and dopa enantiomers as tyrosinase substrates initiating L- and D-melanogenesis pathways. *Biotechnology and Applied Biochemistry, 68*(4), 823-831. https://doi.org/10.1002/bab.1998

Fitzpatrick, R. (2013). *The mom test: How to talk to customers and learn if your business is a good idea when everyone is lying to you*. CreateSpace Independent Publishing Platform.

Goldfeder, M., Kanteev, M., Isaschar-Ovdat, S., Adir, N., & Fishman, A. (2014). Determination of tyrosinase substrate-binding modes reveals mechanistic differences between type-3 copper proteins. *Nature Communications, 5*(1), Article 4505. https://doi.org/10.1038/ncomms5505

Kampatsikas, I., Bijelic, A., & Rompel, A. (2019). Biochemical and structural characterization of tomato polyphenol oxidases provide novel insights into their substrate specificity. *Scientific Reports, 9*, Article 4022. https://doi.org/10.1038/s41598-019-39687-0

Kang, D., Sun, S., Kurnik, M., Morales, D., Dahlquist, F. W., & Plaxco, K. W. (2017). A new architecture for reagentless, protein-based electrochemical biosensors. *Journal of the American Chemical Society, 139*(35), 12113-12116. https://doi.org/10.1021/jacs.7b05953

Klabunde, T., Eicken, C., Sacchettini, J. C., & Krebs, B. (1998). Crystal structure of a plant catechol oxidase containing a dicopper center. *Nature Structural Biology, 5*(12), 1084-1090. https://doi.org/10.1038/4193

Kuijpers, T. F. M., van Herk, T., Vincken, J.-P., Janssen, R. H., Narh, D. L., van Berkel, W. J. H., & Gruppen, H. (2014). Potato and mushroom polyphenol oxidase activities are differently modulated by natural plant extracts. *Journal of Agricultural and Food Chemistry, 62*(1), 214-221. https://doi.org/10.1021/jf4043375

Melamed, E., Glaeser, B., Growdon, J. H., & Wurtman, R. J. (1980). Plasma tyrosine in normal humans: Effects of oral tyrosine and protein-containing meals. *Journal of Neural Transmission, 47*(4), 299-306. https://doi.org/10.1007/BF01247323

Nutt, J. G., Woodward, W. R., Hammerstad, J. P., Carter, J. H., & Anderson, J. L. (1984). The "on–off" phenomenon in Parkinson's disease: Relation to levodopa absorption and transport. *New England Journal of Medicine, 310*(8), 483-488. https://doi.org/10.1056/NEJM198402233100802

Nyholm, D., Odin, P., Johansson, A., Chatamra, K., Locke, C., Dutta, S., & Othman, A. A. (2013). Pharmacokinetics of levodopa, carbidopa, and 3-O-methyldopa following 16-hour jejunal infusion of levodopa-carbidopa intestinal gel in advanced Parkinson's disease patients. *The AAPS Journal, 15*(2), 316-323. https://doi.org/10.1208/s12248-012-9439-1

Panis, F., Kampatsikas, I., Bijelic, A., & Rompel, A. (2020). Conversion of walnut tyrosinase into a catechol oxidase by site-directed mutagenesis. *Scientific Reports, 10*, Article 1659. https://doi.org/10.1038/s41598-020-57671-x

Pettersen, E. F., Goddard, T. D., Huang, C. C., Meng, E. C., Couch, G. S., Croll, T. I., Morris, J. H., & Ferrin, T. E. (2021). UCSF ChimeraX: Structure visualization for researchers, educators, and developers. *Protein Science, 30*(1), 70-82. https://doi.org/10.1002/pro.3943

Prexler, S. M., Frassek, M., Moerschbacher, B. M., & Dirks-Hofmeister, M. E. (2019). Catechol oxidase versus tyrosinase classification revisited by site-directed mutagenesis studies. *Angewandte Chemie International Edition, 58*(26), 8757-8761. https://doi.org/10.1002/anie.201902846

Probst, D., Batchu, K., Younce, J. R., & Sode, K. (2024). Levodopa: From biological significance to continuous monitoring. *ACS Sensors, 9*(8), 3828-3839. https://doi.org/10.1021/acssensors.4c00602

Shao, Z., Wang, P., Zhu, Q., Xu, R., Song, J., Bi, X., Zhang, H., Zhang, M., Li, Y. K., Wu, Y., & Guo, D. (2024). *DeepSeekMath: Pushing the limits of mathematical reasoning in open language models* [Preprint]. arXiv. https://doi.org/10.48550/arXiv.2402.03300

Tesoro, C., Cembalo, G., Guerrieri, A., Bianco, G., Acquavia, M. A., Di Capua, A., Lelario, F., & Ciriello, R. (2023). A critical overview of enzyme-based electrochemical biosensors for L-Dopa detection in biological samples. *Chemosensors, 11*(10), Article 523. https://doi.org/10.3390/chemosensors11100523

UniProt Consortium. (2025). UniProt: The Universal Protein Knowledgebase in 2025. *Nucleic Acids Research, 53*(D1), D609–D617. https://doi.org/10.1093/nar/gkae1010

Virador, V. M., Reyes Grajeda, J. P., Blanco-Labra, A., Mendiola-Olaya, E., Smith, G. M., Moreno, A., & Whitaker, J. R. (2010). Cloning, sequencing, purification, and crystal structure of Grenache (Vitis vinifera) polyphenol oxidase. *Journal of Agricultural and Food Chemistry, 58*(2), 1189-1201. https://doi.org/10.1021/jf902939q

Virtanen, P., Gommers, R., Oliphant, T. E., Haberland, M., Reddy, T., Cournapeau, D., Burovski, E., Peterson, P., Weckesser, W., Bright, J., van der Walt, S. J., Brett, M., Wilson, J., Millman, K. J., Mayorov, N., Nelson, A. R. J., Jones, E., Kern, R., Larson, E., … SciPy 1.0 Contributors. (2020). SciPy 1.0: Fundamental algorithms for scientific computing in Python. *Nature Methods, 17*(3), 261-272. https://doi.org/10.1038/s41592-019-0686-2

Wang, G., Xu, G., Xie, X.-Y., Wang, H.-L., Huang, J.-X., Huang, Z.-S., Qiu, G.-H., Du, Y.-L., Dai, R.-L., Lu, Z.-J., Chen, G., Dong, Q., Zhou, H.-Y., Qin, Y., Li, J., Wang, Y., Shang, H.-F., Chen, X.-W., & Chen, S.-D. (2025). China Parkinson's disease report, 2025. *Journal of Neurology and Neurorehabilitation, 21*(2), 63-98. https://doi.org/10.12022/jnnr.2025-0003

Wurtman, R. J., Chou, C., & Rose, C. M. (1967). Daily rhythm in tyrosine concentration in human plasma: Persistence on low-protein diets. *Science, 158*(3801), 660-662. https://doi.org/10.1126/science.158.3801.660

Zhu, L., Chang, Y., Li, Y., Qiao, M., & Liu, L. (2023). Biosensors based on the binding events of nitrilotriacetic acid–metal complexes. *Biosensors, 13*(5), 507. https://doi.org/10.3390/bios13050507

8. Appendix

A. Screen-Printed Electrode Characterization

C300 electrode configuration

A C300 screen-printed carbon electrode (SPCE) was used as the electrochemical substrate. The electrode measures 36 × 10 × 0.25 mm and integrates a 4 mm-diameter carbon working electrode, a carbon counter electrode, an Ag/AgCl reference electrode, and Ag conductor tracks on a compact disposable strip. This three-electrode configuration permits direct connection to the electrochemical workstation without a separate reference or counter electrode. The screen-printed carbon working surface provides a comparatively large electroactive area for enzyme-film deposition, while the integrated geometry reduces variation in electrode spacing and supports repeatable batch testing.

Electrode preparation and enzyme-recognition principle

For the standard formulation, aqueous trehalose (1 mg mL^{-1}), Triton X-100 (1%), BSA (6 mg mL^{-1}), and PPO at the specified dilution were combined at a 1:1:1:1 volume ratio to form the enzyme mixture. Trehalose was included as a stabilizing excipient, Triton X-100 assisted wetting and coating uniformity, BSA provided a protein-rich cross-linking matrix, and PPO served as the L-DOPA recognition enzyme. Immediately before coating, the enzyme mixture was combined with glutaraldehyde (GA) at a mixture-to-GA volume ratio of 2:1 and mixed thoroughly. Because GA initiates rapid protein cross-linking, the freshly prepared formulation was deposited onto the C300 working area without delay.

The cross-linked formulation was applied in successive aliquots, with each aliquot allowed to air dry before the next was added, until the total enzyme-layer volume reached 5 µL. After the enzyme layer had dried completely, 2.5 µL of 5% waterborne polyurethane (PU) was applied to cover the modified area and was allowed to dry naturally at room temperature. The resulting architecture combined a GA-cross-linked BSA/PPO recognition layer with a hydrated PU outer membrane. PPO catalyzes the oxidation of L-DOPA to dopaquinone; at an applied potential of -0.2 V versus Ag/AgCl, dopaquinone is electrochemically reduced, generating a cathodic current whose magnitude increases with L-DOPA concentration.

A total of 5.00 µL of the freshly cross-linked enzyme formulation was applied to the working-electrode region in five sequential aliquots of 0.25, 0.75, 1.00, 1.50, and 1.50 µL, in that order. Each aliquot was allowed to air dry completely before the next aliquot was added; wet aliquots were not pooled. The electrode was kept level during deposition, and

the ambient temperature, relative humidity, and drying interval for each aliquot were recorded in the batch record.

Electrochemical conditioning, measurement, and data processing

Before amperometric measurement, the modified electrode was immersed in PBS and conditioned by cyclic voltammetry from -0.6 to +0.6 V at 0.05 V s^{-1}. Repeated scanning was continued until successive voltammograms converged, indicating stabilization of the electrode response and sufficient hydration of the PU layer. Chronoamperometry was then performed at -0.2 V for 120 s in L-DOPA solutions of defined concentration. For each trace, the absolute value of the arithmetic mean of the final 20 sampled current points was used as the steady-state response. Each calibration was repeated for at least three independent rounds; the standard PU-coated electrode was tested in four rounds.

Current values recorded in A or µA by different workstations were converted to µA before analysis. Linear regression was performed using the mean steady-state current at each concentration. Error bars on calibration curves represent the standard deviation (SD) among replicate rounds, whereas error bars on sensitivity plots represent the SD of slopes obtained by fitting each round independently. The I-T traces in Figure A3 were smoothed only to improve visual readability; the displayed smoothing was not used for final-20-point extraction, sensitivity calculation, or regression. Therefore, all reported numerical results remain derived from the unmodified experimental data.

Cyclic-voltammetric conditioning of the PU-coated electrode

The complete 20-cycle CV sequence showed a large initial transient followed by progressive contraction and convergence of the voltammetric envelope. The first cycle therefore reflects the strongest initial equilibration and wetting effects, whereas the later scans more closely represent the stabilized electrode. To show the late-stage evolution without compressing the response, selected cycles 5, 10, 15, and 20 are presented separately in Figure A1, while Figure A2 retains all 20 cycles and the full current range.

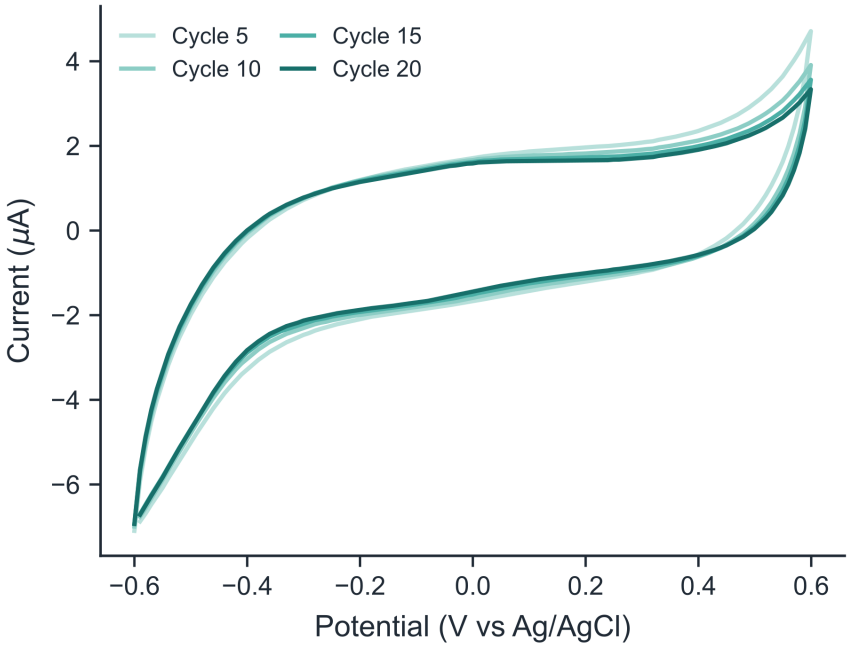


Figure A1. Selected cyclic voltammetry conditioning cycles (5, 10, 15, and 20) recorded in PBS from −0.6 to +0.6 V at 0.05 V s^{-1}.

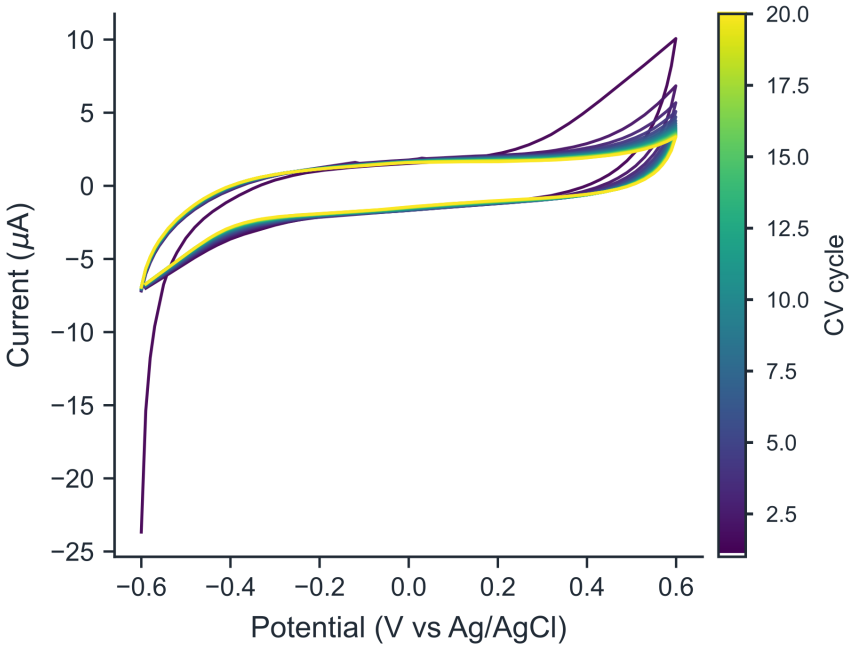


Figure A2. Complete set of 20 cyclic voltammetry conditioning cycles. The broader first-cycle response is retained to show the full stabilization process.

By cycles 19 and 20, the root-mean-square difference between successive current traces was 0.0123 µA, corresponding to only 0.12% of the cycle-20 peak-to-peak current. This small late-cycle difference demonstrates that the combined effects of electrode equilibration and PU hydration had largely stabilized before amperometric calibration. The convergence

criterion also reduces the likelihood that changes in membrane wetting, rather than L-DOPA concentration, dominate the subsequent current response.

Amperometric response and analytical performance of the PU-coated electrode

Mean chronoamperometric current-magnitude traces were obtained for 3, 5, 10, 15, 20, 25, 30, 35, 40, and 50 µM L-DOPA across four calibration rounds. Each trace showed an initially higher current followed by a gradual approach to a quasi-steady response within the 120 s measurement window. The traces remained concentration ordered throughout the measurement: higher L-DOPA concentrations produced consistently higher current magnitudes, supporting concentration-dependent enzymatic conversion and electrochemical readout. Figure A3 lists each concentration explicitly rather than using a continuous color scale.

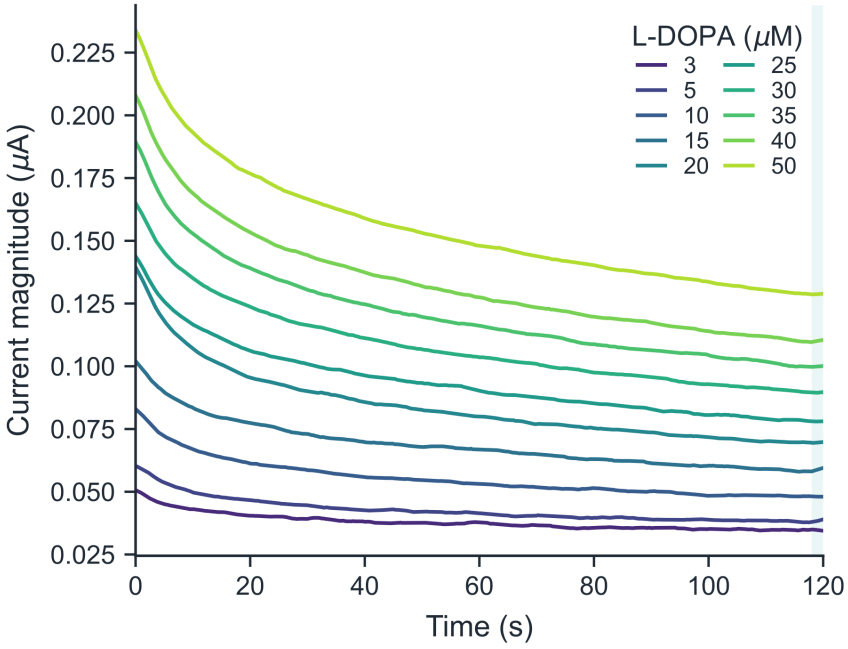


Figure A3. Mean chronoamperometric responses at −0.2 V for 3-50 µM L-DOPA across four calibration rounds. Curves are display-smoothed; quantitative extraction used the original traces.

The standard PU-coated electrode produced a highly linear response from 3 to 50 µM L-DOPA. Fitting the concentration means gave $I = 0.00200964C + 0.0285472$, where I is the steady-state current magnitude in µA and C is the L-DOPA concentration in µM. The corresponding sensitivity was 2.010 nA μM^{-1}, with $R^2 = 0.99962$ and an RMSE of 0.000578 µA. When the four rounds were fitted independently, sensitivity was 2.010 ± 0.045 nA μM^{-1} (mean ± SD). Across the ten calibration concentrations, the between-round coefficient of variation ranged from 0.7% to 4.8%, demonstrating both strong linearity and reproducible response over the tested range.

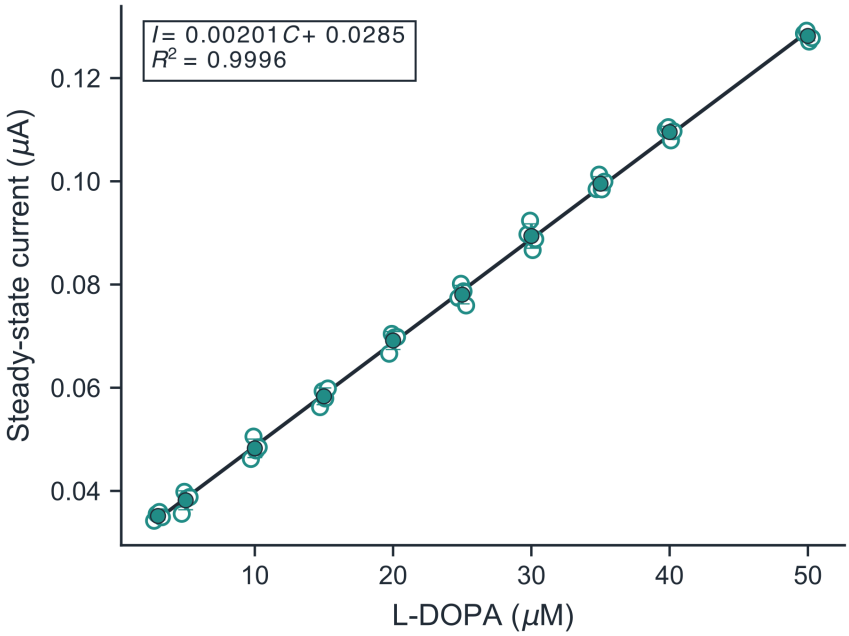


Figure A4. Linear calibration of the standard PU-coated electrode. Symbols show individual measurements from four calibration rounds; the line is the regression fitted to concentration means.

Regression-based theoretical LOD and LOQ

Regression-based theoretical detection and quantitation limits were estimated from the complete 10-level calibration of the standard PU-coated electrode using the ICH Q2(R2) relationships LOD = 3.3σ/S and LOQ = 10σ/S, where S is the calibration slope and σ is the residual standard deviation of the response. For the mean calibration, S = 0.00200964 μA μM^{-1} and $\sigma = [\Sigma(y_i - \hat{y}_i)^2/(n - 2)]^{1/2}$ = 0.000645744 μA (n = 10 concentration levels; 8 residual degrees of freedom). The resulting theoretical LOD was 1.06 μM and the theoretical LOQ was 3.21 μM. These values are regression-based estimates rather than experimentally confirmed limits. They should be verified using independent blank and low-concentration samples, together with accuracy and precision testing near the lower range limit. The same calculation was not applied to the three-level BSA and PPO screening experiments because their single residual degree of freedom would make σ, LOD, and LOQ statistically unstable.

Competition-oriented three-level screening design

The formulation-comparison experiments used a three-level, competition-oriented screening design at low, intermediate, and high L-DOPA concentrations (4, 15, and 45 μM). These levels were selected by the team to span the low, middle, and upper portions of the 3-50 μM measurement range proposed for SensUs 2026 and to simulate a constrained pre-event calibration strategy suitable for a fixed competition timeslot. Because a straight-line

fit through only three concentration levels has one residual degree of freedom, the resulting slope and R^2 values were used only as comparative screening metrics for formulation selection. They demonstrate an apparent concentration-dependent response across the preset competition-oriented conditions, but they do not constitute a formal validation of linearity or analytical range. Formal linearity and range were evaluated only with the full 3-50 µM calibration of the standard PU-coated electrode.

Functional integrity of the cross-linked enzyme layer without the PU outer membrane

To evaluate the underlying enzyme layer independently of the PU barrier, electrodes were prepared using the same cross-linked trehalose/Triton X-100/BSA/PPO formulation but without the final PU overcoat. Three independent calibration rounds in PBS retained a coherent concentration-dependent response from 4 to 45 µM L-DOPA. The fitted sensitivity was 3.734 ± 0.084 nA μM^{-1} across rounds, with R^2 = 0.9940. Between-round coefficients of variation were 1.9-4.2% at the tested concentrations, indicating that the exposed enzyme coating remained functionally responsive during repeated measurements.

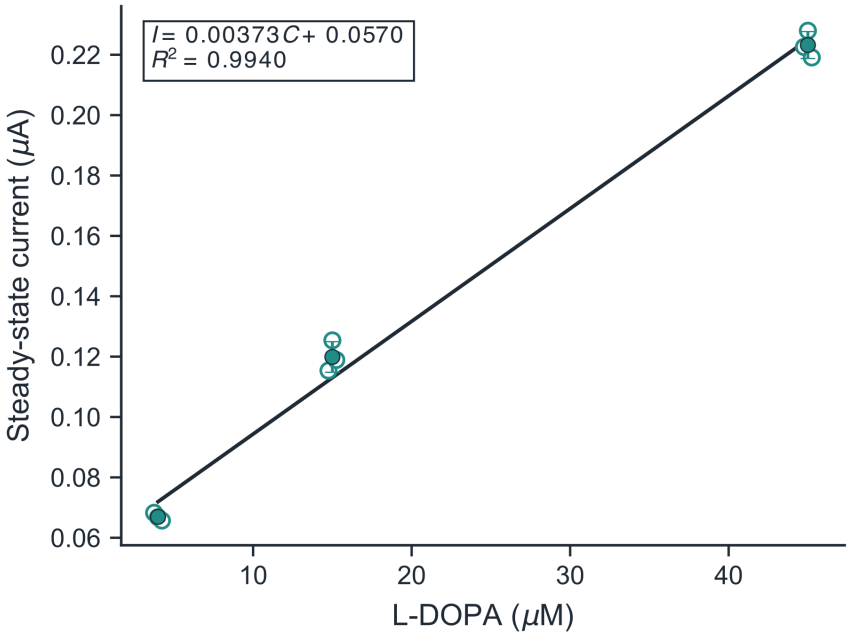


Figure A5. Calibration of the cross-linked enzyme layer without the PU outer membrane. Symbols show individual measurements from three calibration rounds; the line is the regression fitted to concentration means.

The no-PU response was higher than that of the standard PU-coated electrode, which is consistent with removal of an additional diffusion barrier to L-DOPA and dopaquinone. More importantly, the reproducible concentration response across three rounds provides functional evidence that the GA-cross-linked BSA/PPO layer remained attached and active in PBS rather than detaching immediately during measurement. This experiment does not directly quantify protein leaching, dry-film mass, or long-term adhesion; the result is therefore interpreted as evidence of short-term functional integrity rather than a direct measurement of coating retention.

Optimization of BSA concentration

BSA serves as both a stabilizing protein environment and a cross-linkable structural matrix for PPO immobilization. Insufficient BSA may produce a discontinuous or mechanically weak recognition layer, whereas excessive BSA can increase the amount and density of cross-linked protein, lengthen transport paths, and dilute the effective catalytic fraction of the coating. To evaluate this balance, final BSA concentrations of 1, 10, 20, 30, and 40 mg mL^{-1} were compared using three calibration rounds at 4, 15, and 45 µM L-DOPA.

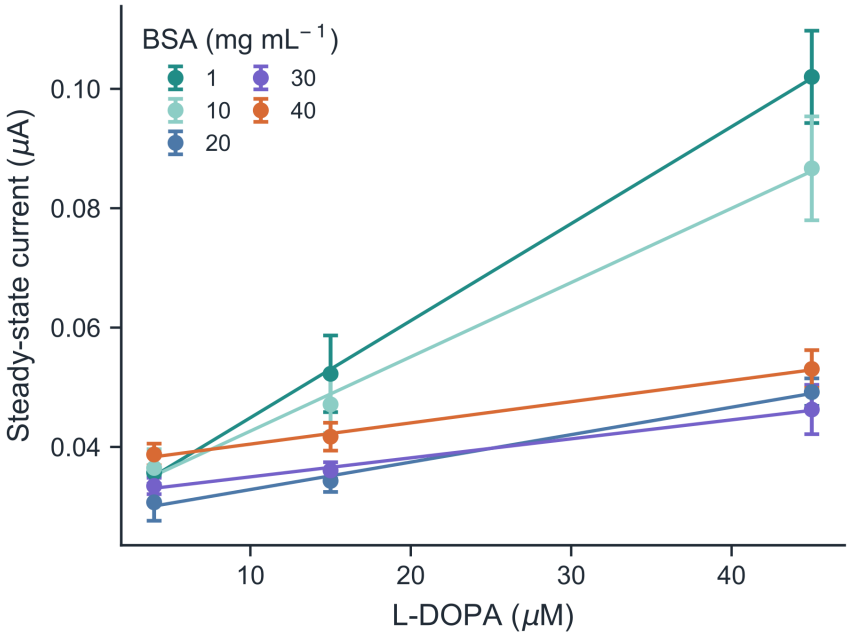


Figure A6. L-DOPA calibration curves for final BSA concentrations of 1, 10, 20, 30, and 40 mg mL^{-1}. Points show mean ± SD across three calibration rounds.

The 1 mg mL^{-1} BSA formulation produced the highest sensitivity, 1.626 ± 0.162 nA μM^{-1}, with R^2 = 0.9996. Sensitivity decreased to 1.244 ± 0.274 nA μM^{-1} at 10 mg mL^{-1} (R^2 = 0.9965), and further decreased to 0.460 ± 0.126, 0.318 ± 0.131, and 0.355 ± 0.110 nA μM^{-1} at 20, 30, and 40 mg mL^{-1}, respectively. The corresponding R^2 values were 0.9940, 0.9952, and 0.9960. Thus, the high-BSA formulations retained an approximately linear concentration dependence but exhibited a 72-80% reduction in sensitivity relative to the 1 mg mL^{-1} condition.

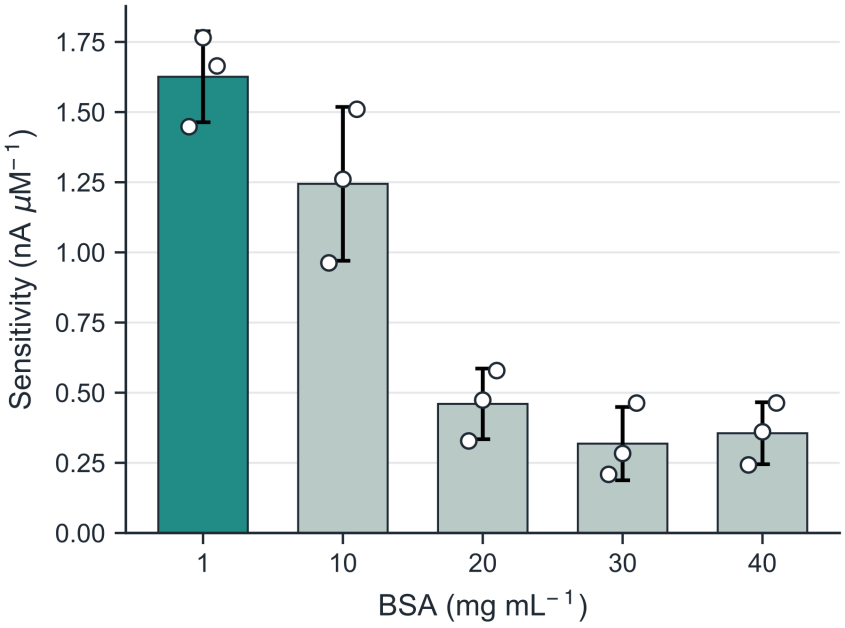


Figure A7. Sensitivity obtained for each BSA concentration. Error bars show the SD of independently fitted round-specific slopes (n = 3); 1 mg mL^{-1} is highlighted.

These results support 1 mg mL^{-1} as the preferred final BSA concentration. The strong attenuation at ≥20 mg mL^{-1} is consistent with accumulation of excess protein in the modified layer, producing a denser cross-linked network that can hinder analyte/product transport and reduce the measured current. Because film thickness and surface morphology were not measured directly in this experiment, the transport and packing explanation should be regarded as a mechanism consistent with the electrochemical trend rather than a direct structural measurement.

Optimization of PPO loading

PPO loading was screened using undiluted enzyme and 2-fold, 4-fold, and 8-fold dilutions. Each condition was assessed in three independent experimental rounds at the same competition-oriented low, intermediate, and high L-DOPA levels. The purpose of this experiment was to characterize how enzyme loading influenced response magnitude, repeatability, and apparent concentration dependence while avoiding an overly concentrated enzyme phase that could dry into a thick, heterogeneous, or particle-rich film. Owing to the limited three-level design, this experiment was treated as a formulation-ranking screen rather than a definitive optimization study.

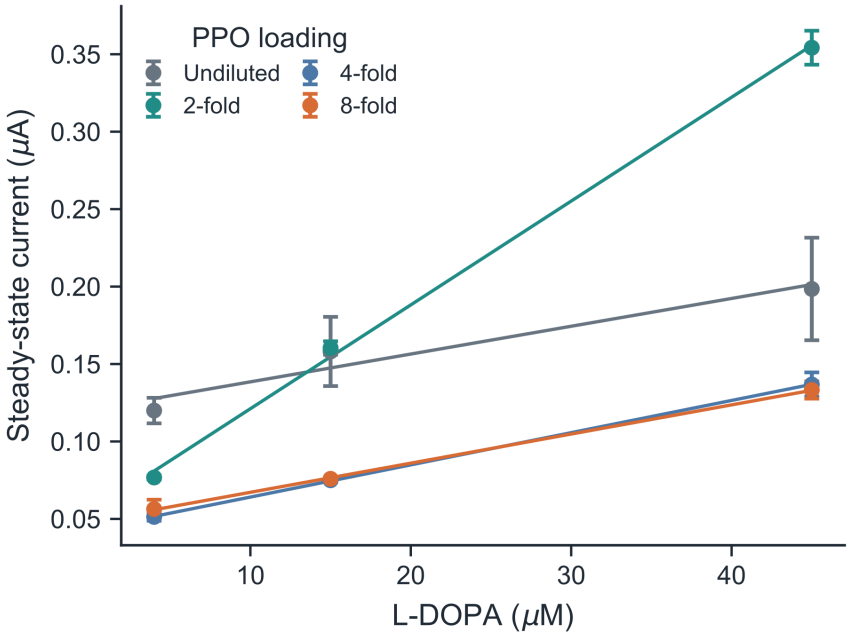


Figure A8. L-DOPA calibration curves for undiluted PPO and 2-fold, 4-fold, and 8-fold PPO dilutions. Points show mean ± SD across three calibration rounds.

The apparent sensitivity depended non-monotonically on PPO loading. The measured sensitivities were 1.795 ± 0.587 nA μM^{-1} for the undiluted formulation, 6.703 ± 0.266 nA μM^{-1} for the 2-fold dilution, 2.079 ± 0.205 nA μM^{-1} for the 4-fold dilution, and 1.882 ± 0.245 nA μM^{-1} for the 8-fold dilution. The corresponding R^2 values were 0.9410, 0.9987, 0.9999, and 0.9998, respectively. These data show that increasing the nominal enzyme concentration did not produce a proportionally stronger or more consistent electrochemical response. Instead, the observed signal was influenced by the combined effects of catalytic loading, film formation, cross-link density, and mass transport.

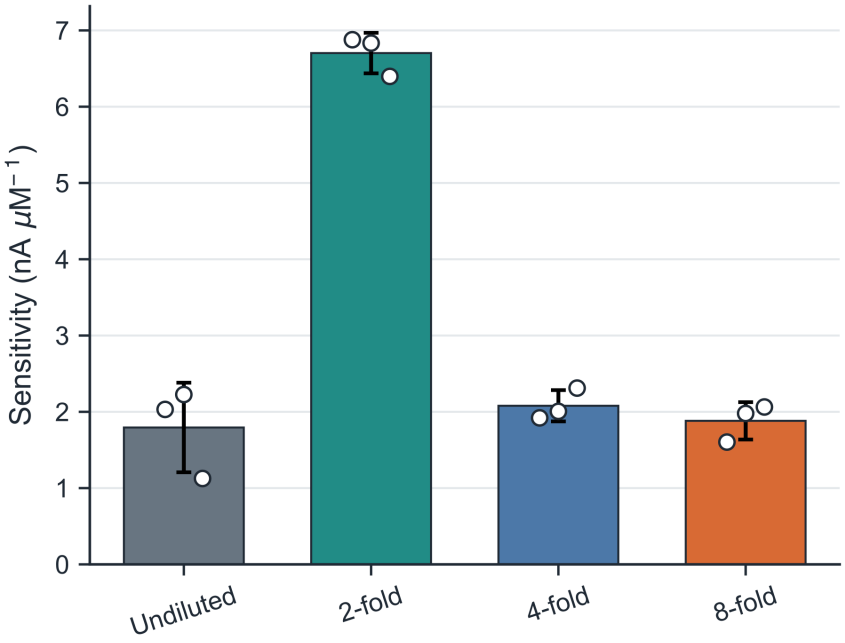


Figure A9. Sensitivity obtained for each screened PPO loading. Error bars show the standard deviation of slopes fitted independently for the three experimental rounds (n = 3). The comparison is presented as a formulation-screening result and does not designate a universally optimal PPO dilution.

Taken together, the screening results support the use of a moderate, empirically controlled PPO loading rather than the assumption that the highest enzyme concentration is necessarily optimal. The three-level data do not establish a single universally optimal dilution. Final formulation selection should also consider between-electrode repeatability, coating uniformity, drying behavior, short-term stability, and performance after PU application.

Materials and reagent identification

The key commercially sourced materials were L-DOPA (catalog number XW015992703), D-(+)-trehalose dihydrate derived from Saccharomyces cerevisiae (catalog number A600966-0025), 1% Triton X-100 aqueous solution (catalog number IR9069-100mL), bovine serum albumin (BSA; catalog number A23088-100G), polyphenol oxidase (PPO; catalog number CP8723-25kU), 10× phosphate-buffered saline (10× PBS; BBI/Sangon Biotech, catalog number E607016-0500, 500 mL), and waterborne polyurethane (PU; Macklin, catalog number W909579-100g, 60% solids, 100 g). The 300-type carbon electrode was obtained from Changsha Sanjun Electronic Technology Co., Ltd. (product/catalog number 300; package size: 100 electrodes). For each experimental batch, the manufacturer, full catalog number, lot number, expiry date, date opened, storage condition, preparation date and time, and operator should be recorded to ensure complete traceability from electrode preparation to the corresponding raw electrochemical data files.

B. Microneedle Sensor Characterization

This appendix aggregates the electrochemical characterisation data supporting the main text: the electrode's linear response to L-DOPA across three physiologically relevant media, an in-vivo continuous monitoring trace in an anaesthetised rat, and a selectivity assessment against six potential interferents. All measurements were performed by chronoamperometry with the working electrode held at −0.2 V vs. Ag/AgCl. All measurements reported in this appendix were performed on microneedle electrodes functionalised with commercial mushroom-derived polyphenol oxidase (PPO); the de novo-designed dicopper catalytic protein described in the main innovation section was not the enzyme deployed in the electrochemical dataset shown here.

B1. Microneedle electrode geometry

The electrode used for the measurements in this appendix is a SUNJEEN ME100 flexible microneedle. The complete electrode is 26.5 mm long and incorporates working, counter, and Ag/AgCl reference electrodes on a flexible substrate. For in vivo measurements, the device was trimmed to provide an insertion segment of approximately 5 mm, placing the working-electrode region in contact with subcutaneous interstitial fluid (Figure B1).

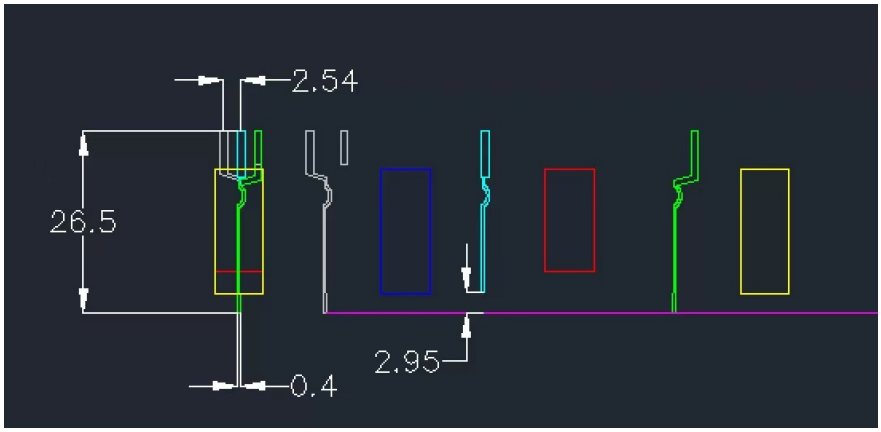


Figure B1. Original geometry drawing of the SUNJEEN ME100 flexible microneedle electrode before trimming, showing the front and side dimensions.

B2. Enzyme-modification protocol

The working electrode was modified by drop-casting a freshly prepared enzyme mixture in seven layers, followed by dip-coating in aqueous polyurethane. Commercial mushroom-derived polyphenol oxidase (L-DOPA-active) was first weighed and dissolved in deionised water to a 200 U/µL mother solution and then diluted eight-fold to a 25 U/µL working solution. The working solution was combined with four standard stock solutions in the fixed volume ratio listed in Table B1, and the resulting mix was drop-cast within minutes of preparation to prevent glutaraldehyde-driven premature cross-linking. Each electrode received one initial layer of 0.25 µL followed by six layers of 0.5 µL, for a total of 3.25 µL per electrode; each layer was air-dried at room temperature until the film became matte and non-flowing before the next layer was applied. After the final layer had dried, the electrode was trimmed to length and dip-coated three times in a 30 wt.% aqueous polyurethane dispersion, air-drying between dips.

Table B1. Enzyme-mix formulation for the drop-cast layer. Components are combined by volume in the ratio shown; a fresh mix is made immediately before use. Per-electrode volumes are 0.25 µL for the first layer plus 0.5 µL for each of the six subsequent layers (3.25 µL in total).

Stock solution	Concentration	Volume ratio
L-DOPA-oxidising enzyme working solution	25 U/µL	1
Bovine serum albumin (BSA)	6 mg/mL	1
Trehalose	1 mg/mL	1
Triton X-100	1% (v/v)	1
Glutaraldehyde (GLA)	1% (v/v)	2
Total		6

B3. Test media preparation

The three media used in the L-DOPA calibration were prepared as follows. PBS was standard 0.01 M phosphate-buffered saline at pH 7.4. Simulated interstitial fluid was made by mixing one volume of human serum with two volumes of PBS in a 1 : 2 (v/v) ratio, giving an approximately physiological electrolyte and protein background against which the serum-matrix influence on the enzymatic–electrochemical readout could be assessed.

The skin-mimicking gel calibration series was prepared in two steps and combined at final volume. First, a 10 mM L-DOPA stock was prepared by dissolving 19.7 mg L-DOPA powder in 10 mL 0.01 M PBS (pH 7.4) protected from light, with 0.1 mg/mL ascorbate added as an antioxidant. The stock was serially diluted in PBS to give a 2× concentration series (50, 25, 12.5, 6.25 and 0 µM). Second, a 2× agarose stock at 3% (w/v) was prepared by dissolving 3.0 g agarose in 100 mL PBS with heating until clear, then held at 50 °C. Equal volumes of the 2× L-DOPA series and the 2× agarose stock were rapidly mixed 1 : 1 to give the final calibration series in 1.5% agarose gel (Table B2). The 50 µM point was prepared but excluded from the downstream analysis and does not appear in Figure B2c; the retained points therefore cover 0-25 µM.

Table B2. Skin-mimicking gel calibration series after 1:1 mixing of the 2× L-DOPA dilution series with 2× (3% w/v) agarose stock at 50 °C. The final calibration series covers 0-25 µM in 1.5% agarose. The 50 µM entry from the original preparation table was excluded from the fit shown in Figure B2c.

Target L-DOPA (µM)	2× L-DOPA solution	3% agarose solution	Final composition
25	10 mL of 50 µM stock	10 mL	1.5% agarose / 25 µM
12.5	10 mL of 25 µM stock	10 mL	1.5% agarose / 12.5 µM
6.25	10 mL of 12.5 µM stock	10 mL	1.5% agarose / 6.25 µM
0	10 mL of PBS blank	10 mL	1.5% agarose / 0 µM

B4. Linear response across three media

The microneedle electrode was calibrated in three media that progressively better mimic the subcutaneous environment: phosphate-buffered saline (PBS), a simulated interstitial fluid based on diluted serum, and a hydrogel matrix that approximates skin transport properties. In PBS the response is highly linear from 0.156 to 10 µM with slope 0.226 nA/µM and R^2 = 0.998, covering the full clinical L-DOPA window. Using the 0 µM level (σ_blank = 0.137 nA, n = 4), the regression-based estimate was LOD = 3σ_blank/S = 1.82 µM. In simulated interstitial fluid the response remains linear from 6.25 to 50 µM with slope 0.140 nA/µM and R^2 = 0.996, confirming that serum matrix components do not disrupt the enzymatic–electrochemical readout. In the skin-mimicking gel the response is still monotonic across 0-25 µM but with a much lower slope of 0.047 nA/µM and a reduced R^2 of 0.988, reflecting slower substrate diffusion and greater point-to-point scatter in the gel matrix. Slope, intercept, and R^2 are annotated in each panel of Figure B2.

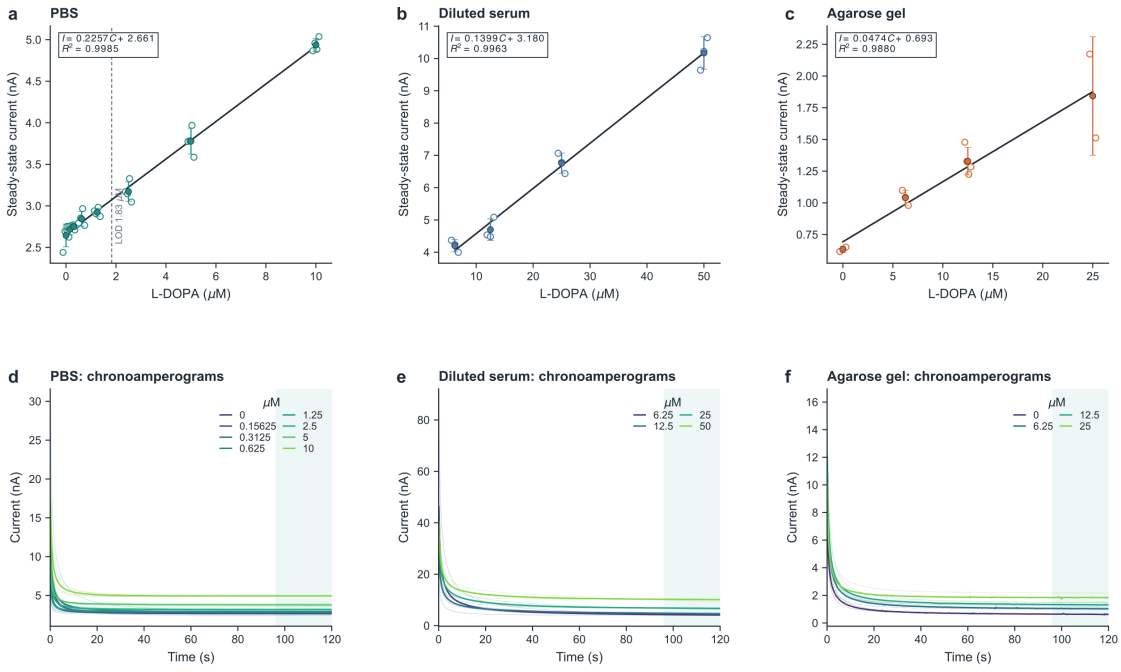


Figure B2. Calibration and raw chronoamperometry of the microneedle electrode in three media. (a-c) Concentration–current calibration in PBS, diluted serum, and agarose gel, respectively. (d-f) Corresponding chronoamperograms; shaded regions indicate the steady-state windows used for current extraction.

B5. In-vivo continuous monitoring in an anaesthetised rat

The fully modified microneedle was implanted subcutaneously in an anaesthetised SD rat and polarised continuously at −0.2 V vs. Ag/AgCl. After a baseline round, L-DOPA was administered by intraperitoneal injection at t = 0, and one 170-second chronoamperometry round was recorded every three minutes for approximately 60 minutes. Figure B3 plots the stable current from the last 20% of each round against time; the red dashed line marks the injection. The electrode captured a rapid post-injection rise in interstitial-fluid L-DOPA followed by the expected decay over the pharmacokinetic window. Rounds coinciding with blood withdrawal for validation sampling introduced fluid-level artefacts and are shown as faded markers with dashed connectors across them.

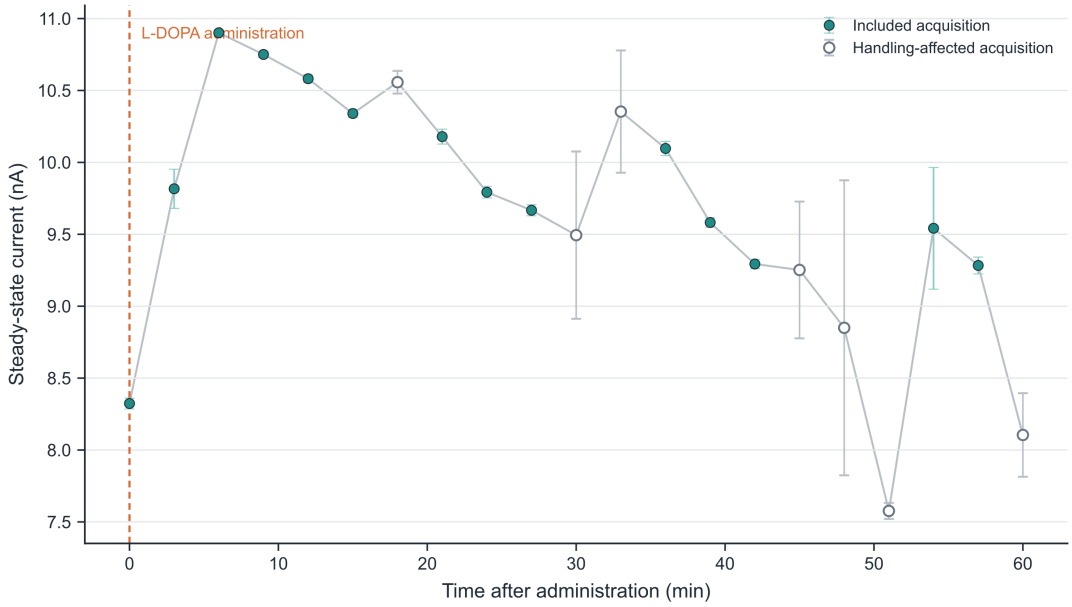
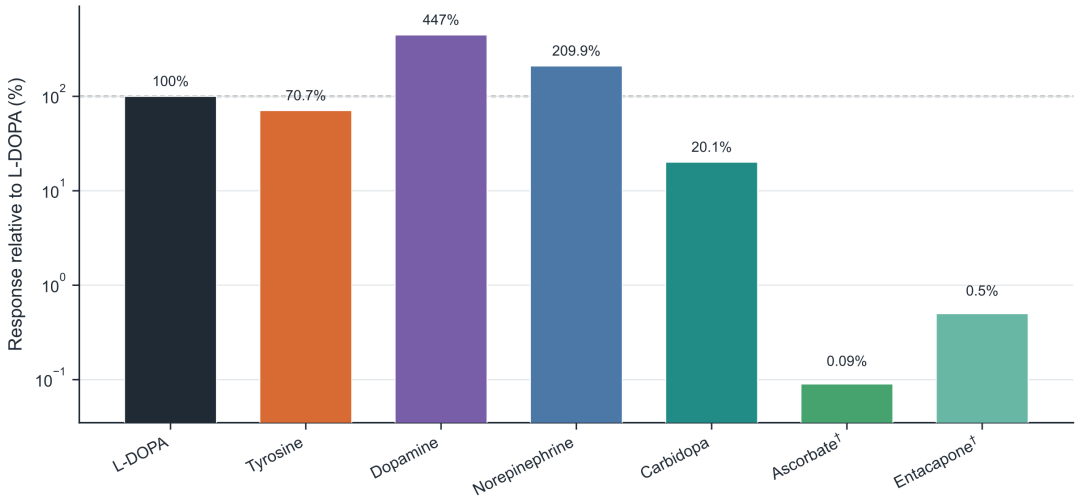


Figure B3. Continuous in vivo chronoamperometry after L-DOPA administration. Each marker represents the steady-state current from one acquisition; open markers denote handling-affected acquisitions.

B6. Selectivity against major interferents

Selectivity was quantified by measuring the electrode response to each potential interferent and comparing its per-µM sensitivity to the L-DOPA per-µM sensitivity measured on the same electrode. Six compounds were tested: L-tyrosine (the direct enzymatic precursor to L-DOPA), dopamine and norepinephrine (structurally similar catecholamines and metabolites), carbidopa (the co-administered peripheral AADC inhibitor), ascorbate (a common electroactive interferent in body fluids), and entacapone (a co-administered COMT inhibitor). Figure B4 summarises the per-µM sensitivity of each interferent expressed as a percentage of the L-DOPA per-µM sensitivity, so that L-DOPA is fixed at 100% for reference.



In the primary protocol, applied to L-tyrosine, dopamine, norepinephrine, and carbidopa, the same physical electrode was first calibrated against L-DOPA in PBS across four concentration levels (typically 6.25-50 µM) to obtain that electrode's own L-DOPA reference slope, kL (nA per µM L-DOPA). Independent 170-second chronoamperometry rounds were then run at a graded series of interferent concentrations, with several rounds and independent batches per concentration. For each interferent concentration cint, the current change ΔI relative to the interferent-free baseline was converted into an L-DOPA-equivalent concentration by ceq = ΔI/kL, and the per-µM sensitivity relative to L-DOPA was reported as 100% × ceq/cint. In the secondary protocol, used to screen ascorbate and entacapone, a single continuous chronoamperometric recording was made in PBS while each interferent was injected sequentially and allowed to equilibrate for 120-200 s at each addition. Because this protocol delivered only one addition point per interferent, the resulting sensitivity ratios are qualitative screens rather than full concentration–response curves.

Figure B4. Per-µM sensitivity to each interferent, normalised to the L-DOPA sensitivity measured on the same microneedle electrode. The y-axis is logarithmic; daggers denote single-addition screens.

B7. Inhibition test—3-O-methyldopa (3-OMD)

3-O-methyldopa (3-OMD) is the principal peripheral metabolite of L-DOPA generated by catechol-O-methyltransferase (COMT). Circulating 3-OMD reaches concentrations of the same order or higher than L-DOPA itself in Parkinson's patients on chronic L-DOPA therapy — reported Cavg ≈ 17 µg/mL (~ 80 µM) for 3-OMD versus ≈ 2.9 µg/mL (~ 15 µM) for L-DOPA on continuous L-DOPA / carbidopa infusion, a roughly six-fold excess (Nyholm et al., 2013) — so a specific test of whether 3-OMD either produces its own electrode signal or inhibits the L-DOPA response was carried out. Because 3-OMD is a methylated catechol, its direct electrochemical activity at the enzyme layer is expected to be low, but as a structural analogue of L-DOPA it could conceivably compete for the polyphenol-oxidase active site and depress the L-DOPA sensitivity. The measurement therefore consists of three chronoamperometric arms recorded on the same microneedle electrode at −0.2 V vs. Ag/AgCl (steady-state current = mean of the last 20% of each 120 s round; n = 2 rounds per concentration for the two L-DOPA arms, n = 1 for the 3-OMD-alone arm): (i) a plain L-DOPA calibration at 6.25, 12.5, 25 and 50 µM as the control; (ii) an L-DOPA calibration over the same range but with a fixed background of 12.5 µM 3-OMD in every sample, testing for competitive inhibition of the L-DOPA response; and (iii) a 3-OMD-only sweep at 6.25, 12.5, 25 and 50 µM to look for any direct 3-OMD signal at the electrode.

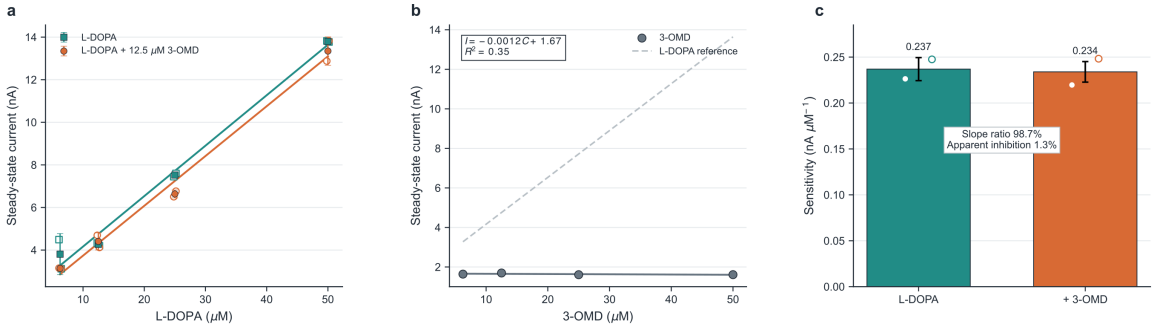


Figure B5. 3-OMD inhibition test at −0.2 V vs. Ag/AgCl. (a) L-DOPA calibration curves with and without a 12.5 µM 3-OMD background; the two calibration lines are essentially superimposed. (b) 3-OMD alone across 6.25-50 µM produces an almost flat current trace (slope ≈ 0 nA/µM) compared with the L-DOPA reference slope (dashed line). (c) Sensitivity slope comparison: the L-DOPA slope in the presence of 12.5 µM 3-OMD is 98.7% of the L-DOPA-alone slope, i.e. an apparent inhibition of only 1.3%, well within run-to-run variability. Error bars in (a) are ± SD of n = 2 replicates per point; bar-chart error bars in (c) are propagated slope uncertainties from the linear fits.

Taken together, the three arms give a consistent picture: 3-OMD is essentially electrochemically silent at the operating potential (fit slope −0.001 nA/µM, R^2 = 0.35, i.e. flat within noise, and the residual ~0.09 nA drift over the tested range is equivalent to only ~0.4 µM of L-DOPA), and it does not inhibit the enzymatic response to L-DOPA in any practically meaningful way (slope ratio 98.7%, apparent inhibition 1.3%, well below the fit-slope uncertainty of ~5%). We therefore treat 3-OMD as a non-interfering species for the intended L-DOPA readout.

B8. Physiological impact of interferents

Per-μM sensitivity alone overstates the practical impact of most interferents, because their physiological or on-medication concentrations differ from L-DOPA by several orders of magnitude. Table B3 combines the measured per-μM sensitivity with reported physiological concentrations of each species to estimate the L-DOPA-equivalent signal contribution one would expect during continuous monitoring, and expresses this contribution as a relative error on a representative L-DOPA target of 5 μM.

Table B3. Physiological impact estimate for each interferent. The per-μM sensitivity is combined with typical circulating or on-medication concentrations to give an expected L-DOPA-equivalent contribution, then expressed as a relative error on a representative 5 μM L-DOPA target. † Sensitivity for these two entries is derived from a single-shot addition test (n = 1, PBS background) rather than a full concentration–response sweep.

Interferent	Per-μM sensitivity vs L-DOPA	Typical physiological / on-medication concentration	Expected L-DOPA-equivalent contribution	Relative to 5 μM L-DOPA
L-Tyrosine	≈ 70% (saturating; measured 3.1 μM equiv per 100 μM Tyr)	40-90 μM in plasma and ISF (not appreciably altered by L-DOPA therapy)	≈ 1.9-2.8 μM equiv	≈ 38-56%
Dopamine (free)	≈ 450%	≤ 5 nM in on-medication plasma (peripheral AADC blocked by carbidopa)	≈ 0.02 μM equiv	≈ 0.4%
Norepinephrine (free)	≈ 210%	1-5 nM in plasma	≈ 0.01 μM equiv	≈ 0.2%
Carbidopa	≈ 20%	1-3 μM plasma peak on standard L-DOPA / carbidopa regimen	≈ 0.2-0.6 μM equiv	≈ 4-12%
Ascorbate†	≈ 0.09%	20-100 μM in plasma and ISF	≈ 0.02-0.09 μM equiv	≈ 0.4-1.8%
Entacapone†	≈ 0% (below noise)	5-10 μM plasma peak on standard COMT-inhibitor regimen	≈ 0	≈ 0%

Two conclusions follow. First, the two catecholamines with per-μM sensitivity at or above L-DOPA — dopamine and norepinephrine — are effectively rejected by physiology rather than by the electrode: their free-plasma concentrations sit in the low nanomolar range, so that even a several-fold per-molecule sensitivity translates into a signal well below one percent of a 5 μM L-DOPA target. Carbidopa and ascorbate reach micromolar levels but their per-μM sensitivity is already low, and entacapone does not respond above baseline

noise, so all three contribute at or below the mid-single-digit percent level. Second, L-tyrosine is the one interferent that the electrode cannot fully exclude: its per-μM response is comparable to L-DOPA, its physiological concentration in plasma and interstitial fluid is orders of magnitude higher than L-DOPA, and its concentration is not suppressed by the standard L-DOPA / carbidopa regimen. In the monitored L-DOPA range this translates into a residual relative contribution of roughly 40-60%, which is the dominant source of chemical interference in the present design and the primary target for future selectivity improvement, most naturally through the de novo-designed dicopper catalytic protein whose active-site geometry is intended to reject the single-phenol tyrosine substrate.

C. De Novo Design of Dicopper Catalytic Proteins

Natural PPO Screening and Selection of the Design Strategy

We first screened ten natural polyphenol oxidase (PPO) candidates for purification and L-DOPA oxidation activity. Five candidates yielded purified protein. Three showed measurable specific activity, whereas PPO6 and pPPO were recorded as having no detectable activity. The remaining five candidates were not purified and therefore were not assayed for activity (Table S1). The highest activity was observed for 1-IPOBA at 155.522 U mg^{-1}, while 2-IPOBA and VIT1 showed substantially lower activities. These results illustrate the limited experimental tractability of the natural-enzyme route in the prokaryotic expression system used here. Bacterial production of active plant PPOs is sensitive to construct boundaries, expression temperature, copper supplementation, and folding assistance, which can constrain rapid experimental iteration (Dirks-Hofmeister et al., 2013).

Table S1. Raw screening records for natural PPO candidates.

Candidate	Source	Purified	Specific activity (U mg^{-1})	Reference
1-IPOBA	Sweet potato	Yes	155.5222	Klabunde et al., 1998 (Q9ZP19)
2-IPOBA	Sweet potato	Yes	2.4385	UniProt Consortium, 2025 (Q9MB14)
VIT1	*Vitis vinifera*	Yes	5.9823	Virador et al., 2010
xPPO	Apricot	No	NA	Derardja et al., 2017
PPO6	Dandelion	Yes	NA	Prexler et al., 2019
PPO7	Dandelion	No	NA	Prexler et al., 2019
pPPO	Potato	Yes	NA	Kuijpers et al., 2014
jrPPO	Walnut	No	NA	Panis et al., 2020
tobacco PPO	Tobacco	No	NA	Broothaerts et al., 2000
SlPPO	*Solanum lycopersicum*	No	NA	Kampatsikas et al., 2019

Note: candidate names, purification status, and numerical activity values reproduce the original screening workbook. NA denotes a blank activity entry. For PPO6 and pPPO, purified protein was obtained but no activity value was recorded; for candidates that were not purified, activity was not assayed.

We therefore moved from searching for the most active natural PPO to de novo protein design for the sensing task. An electrochemical biorecognition element must generate a resolvable L-DOPA catalytic signal after immobilization while reducing cross-reactivity toward tyrosine. We retained the catalytic dicopper pocket of a natural type-3 copper protein and regenerated the surrounding backbone and sequence, combining a structurally defined natural active site with the broader scaffold space accessible to de novo design.

Functional Motif Derived from a Natural PPO

The design started from Bacillus megaterium tyrosinase (TyrBm; UniProt B2ZB02). PDB 4P6S provides the crystallographic background for L-DOPA binding to TyrBm (Goldfeder et al., 2014). The coordinates used for backbone generation, however, were not excised directly from the crystal structure. They were extracted from an AlphaFold 3 co-folded model containing TyrBm, two copper ions, a peroxide bridge, and L-DOPA (Abramson et al., 2024). The extracted atomic motif retained the complete backbones and side chains of the six copper-coordinating histidines, both copper ions, two individual peroxide oxygen atoms, and the complete L-DOPA molecule (Figure C1).

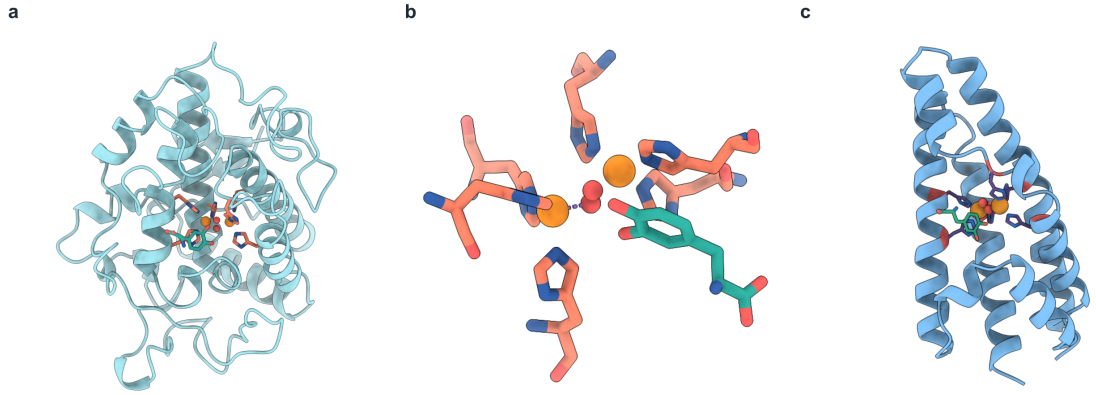


Figure C1. Structural basis of the de novo design route. (a) TyrBm co-folded complex. (b) Extracted dicopper functional motif. (c) AlphaFold 3-predicted Design 15 complex. Copper-coordinating histidines and L-DOPA are shown as sticks; copper and peroxide oxygen atoms are shown as spheres. Structures were rendered in UCSF ChimeraX (Pettersen et al., 2021).

These coordinates were used as geometric conditions for structure generation and do not establish a specific transition state or a complete catalytic mechanism.

Locked Natural-Pocket Design Workflow

The natural-pocket route comprised motif conditioning, RFdiffusion3 backbone generation, LigandMPNN sequence design, AlphaFold 3 structure prediction, computational filtering, PLACER ensemble evaluation, and manual structural review (Figure 4). This section describes the locked workflow that produced the currently active candidates and was used for subsequent sampling. The 33 candidates submitted for experimental evaluation arose from several rounds of workflow iteration. Earlier exploratory batches included alternative local coordinate versions; their original identifiers are retained in the results tables but are not presented as part of the final natural-pocket method.

Backbone Generation

RFdiffusion3 used the atomic coordinates of the six complete histidines, two Cu ions, PER, and DAH as a fixed motif and generated single-chain protein backbones around it (Butcher

et al., 2025). In the locked p392 natural-pocket route, target length was restricted to 135-165 aa. Covalent connectivity and atom identity within the functional motif were preserved during generation. All subsequent models were assessed with common geometric metrics for reproduction of the starting motif.

Sequence Design

LigandMPNN generated eight sequences per backbone with a sampling temperature of 0.2 and random seed 7 (Dauparas et al., 2025). Logit biases of -2.0 and +0.5 were applied to alanine and lysine, respectively. Histidine and cysteine were excluded from all designed positions except the six fixed histidines. Lysine was disallowed at any designed position whose Cα atom was within 10 Å of any Cu, PER, or DAH atom to reduce the likelihood that immobilization chemistry would perturb the catalytic pocket. LigandMPNN explicitly considered the non-protein atomic environment, and the three sequences with the highest ligand-confidence scores were retained for each backbone.

Structure Prediction and Geometric Filtering

Candidate complexes were predicted with AlphaFold 3 without MSAs or templates (Abramson et al., 2024). Each input comprised protein chain A, two independent Cu chains B and C, PER chain D, and DAH chain E. Random seeds 1, 2, and 3 were used, with five samples per seed, yielding 15 models per candidate. The highest-confidence model satisfying the geometric constraints was retained for further evaluation.

The predefined geometric thresholds were motif-atom RMSD < 1.20 Å, side-chain RMSD of the six histidines < 1.80 Å, Cu–Cu distance of 3.00-4.30 Å, maximum His–Cu coordination distance < 3.00 Å, and minimum catechol-O–PER-O distance < 4.00 Å. Immobilization accessibility required no lysine NZ atom within 8 Å of the catalytic core and at least three lysine side chains with solvent-accessible surface area ≥ 25 Å^2.

Substrate Access and Conformational-Ensemble Evaluation

To reduce the risk of burying L-DOPA within the protein, solvent-accessible surface area (SASA) was calculated for the complete DAH molecule and its amino-acid side tail. The locked thresholds were DAH SASA ≥ 75 Å^2, tail SASA ≥ 70 Å^2, tail/free SASA ≥ 0.40, open-ray fraction ≥ 0.24, and maximum open-cone fraction within a 60° half-angle cone ≥ 0.84. One thousand Fibonacci-sphere rays were sampled from the geometric center of the DAH N/O/OXT atoms over a radial range of 2-12 Å. A ray was classified as open when the distance from its centerline to every protein heavy atom remained > 2.5 Å. The open-cone metric

was the largest fraction of open rays within any 60° half-angle cone. These metrics are operational geometric definitions for maintaining substrate access and are not criteria for a catalytic mechanism.

Structures passing these filters were evaluated with PLACER using 100 local conformational samples and DAH as the predicted ligand (Anishchenko et al., 2025). The best pRMSD of the complete DAH molecule across the local samples was reported; the current operational cutoff is ≤ 1.80 Å, although this criterion was not used to remove historically ordered proteins. Finally, unaligned AlphaFold 3 models and motif-aligned structures were reviewed manually to exclude non-compact folds, atomic clashes, obstructed substrate access, and closure by terminal or loop regions, while retaining diverse backbone topologies.

Computational Feasibility

Thirty-three candidates were selected for experimental evaluation: 6 in Batch 1, 13 in Batch 2, and 14 in Batch 3. Selection for experimental evaluation means that a candidate passed the computational review applied in its design round and was submitted for wet-lab testing; it does not imply that all 33 candidates have been experimentally tested or shown to be active.

Under a unified retrospective review, all 33 candidates satisfied the five core geometric thresholds. Motif RMSD ranged from 0.246 to 0.890 Å, histidine side-chain RMSD from 0.600 to 1.613 Å, Cu–Cu distance from 3.316 to 4.259 Å, maximum His–Cu distance from 1.969 to 2.891 Å, and minimum catechol-O–PER-O distance from 1.874 to 3.723 Å (Figure C2; Table S2). Each designed core sequence contained exactly six histidines. A verifiable PLACER best pRMSD was unavailable for C05 and is reported as NA without imputation.

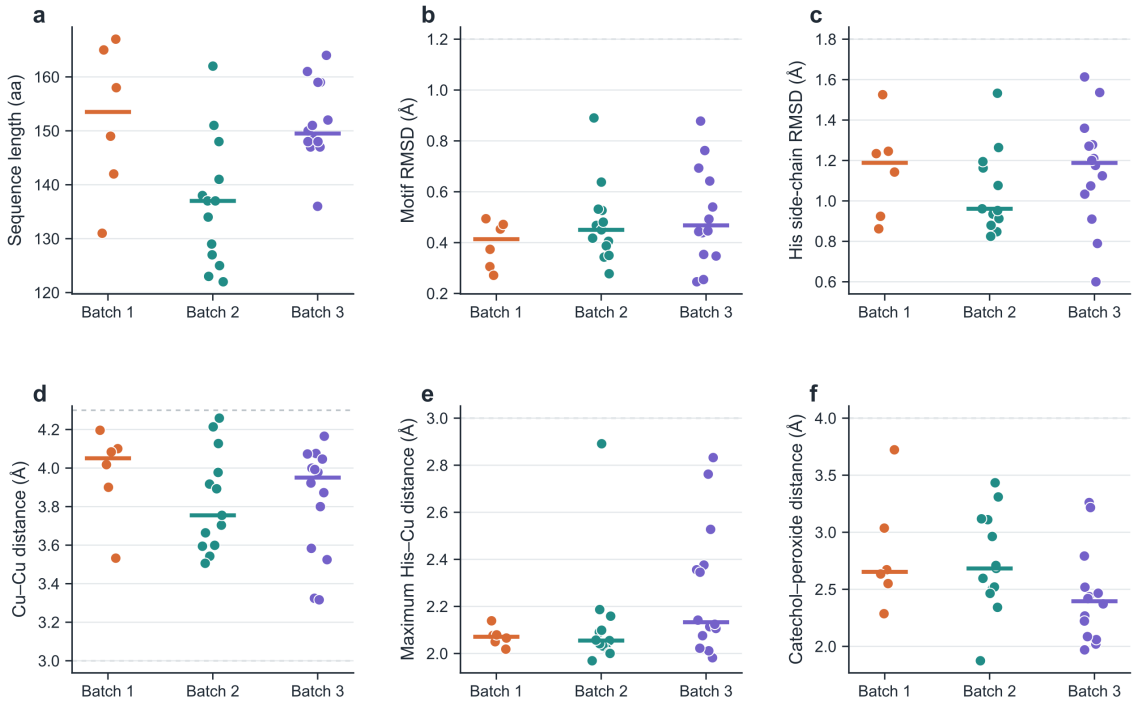


Figure C2. Computational structural distributions for the 33 candidates selected for experimental evaluation. (a) Sequence length. (b) Motif RMSD. (c) Histidine side-chain RMSD. (d) Cu–Cu distance. (e) Maximum His–Cu distance. (f) Minimum catechol–peroxide distance. Orange, teal, and purple denote Batches 1-3; horizontal bars indicate batch medians and dashed lines indicate predefined thresholds.

Table S2. Structural metrics for the 33 experimental candidates.

ID	Candidate	Batch	Length (aa)	Motif RMSD (Å)	His RMSD (Å)
C01	design_6	Batch 1	149	0.306	1.525
C02	design_17	Batch 1	158	0.453	1.234
C03	design_15	Batch 1	142	0.374	1.143
C04	design_5	Batch 1	131	0.271	0.862
C05	design_23	Batch 1	165	0.494	1.246
C06	design_18	Batch 1	167	0.471	0.924
C07	repro_r49_p392	Batch 2	138	0.890	1.532
C08	repro_r40_p392	Batch 2	125	0.468	0.935
C09	repro_r24_p392	Batch 2	141	0.278	0.965
C10	repro_r12_p373	Batch 2	127	0.450	0.847
C11	repro_r08_p373	Batch 2	123	0.405	0.913
C12	repro_r03_p373	Batch 2	134	0.343	1.076
C13	GLA_design1_p373_PLACER1.53	Batch 2	137	0.387	0.879
C14	GLA_design3_p373_PLACER1.63	Batch 2	129	0.417	0.961
C15	GLA_design5_p373_PLACER1.67	Batch 2	162	0.527	1.163
C16	GLA_design14_p392_PLACER1.66	Batch 2	151	0.638	1.264
C17	GLA_design20_p392_PLACER1.80	Batch 2	122	0.350	0.825
C18	big_w20_p373_PLACER1.77	Batch 2	148	0.532	1.194
C19	big_w32_p392_PLACER1.77	Batch 2	137	0.481	0.952
C20	r01_p373	Batch 3	152	0.246	0.789
C21	r03_p373	Batch 3	149	0.353	0.600
C22	r05_p373	Batch 3	147	0.439	0.910
C23	r06_p373	Batch 3	147	0.443	1.278
C24	r07_p373	Batch 3	150	0.540	1.271
C25	r10_p392	Batch 3	148	0.255	1.033
C26	r13_p392	Batch 3	148	0.347	1.124
C27	r18_p392	Batch 3	136	0.446	1.210
C28	r21_p392	Batch 3	164	0.490	1.176
C29	r22_p392	Batch 3	159	0.492	1.074
C30	r24_p392	Batch 3	159	0.642	1.536
C31	r26_p392	Batch 3	136	0.693	1.359
C32	r27_p392	Batch 3	151	0.762	1.200

ID	Candidate	Batch	Length (aa)	Motif RMSD (Å)	His RMSD (Å)
C33	r28_p392	Batch 3	161	0.878	1.613

Table S2 (continued). Metal-site and substrate-geometry metrics.

ID	Cu–Cu (Å)	Max His–Cu (Å)	Catechol-PER (Å)	PLACER best pRMSD (Å)
C01	4.196	2.077	3.036	2.550
C02	4.101	2.139	2.672	1.833
C03	4.084	2.018	2.550	1.859
C04	4.018	2.050	2.634	2.320
C05	3.900	2.066	3.723	NA
C06	3.532	2.079	2.286	2.681
C07	3.917	2.891	2.963	0.651
C08	3.599	2.055	2.506	1.975
C09	3.892	2.021	2.596	1.705
C10	3.542	2.032	1.874	1.280
C11	4.214	2.042	3.110	1.786
C12	4.127	2.003	3.434	1.713
C13	3.704	2.091	2.683	1.772
C14	3.664	2.000	2.520	1.282
C15	3.755	1.969	3.118	1.912
C16	3.594	2.187	3.309	1.681
C17	3.977	2.099	2.709	1.354
C18	4.259	2.159	2.342	1.396
C19	3.506	2.057	2.464	1.948
C20	4.076	1.982	2.372	1.540
C21	4.165	2.114	2.519	1.411
C22	4.073	2.527	1.969	1.280
C23	3.800	2.011	2.792	1.511
C24	3.872	2.106	2.436	1.324
C25	3.979	2.076	3.260	1.717
C26	4.047	2.376	2.419	1.122
C27	3.999	2.022	2.020	1.500
C28	3.583	2.356	2.267	1.519
C29	3.993	2.345	2.059	1.592
C30	3.922	2.124	2.086	1.794
C31	3.324	2.832	2.466	1.576
C32	3.525	2.142	2.222	1.489
C33	3.316	2.762	3.216	1.672

Note: candidate names retain the original workflow identifiers. p392 denotes the natural TyrBm co-folded pocket coordinates, whereas p373 denotes an alternative local coordinate version used during earlier exploration. All candidates with detected activity originated from the p392 route. PLACER best pRMSD was not one of the five uniformly recalculated geometric gates shown in Figure C2; PLACER and pocket-access rules evolved between design rounds.

Table S3. Designed core sequences of the 33 experimental candidates.

ID	Candidate	Length (aa)	Designed core sequence
C01	design_6	149	MTLEEAKAAA AAWVADVQAA LDAKTAAIAA WTPADEEERL ARDAVLAHAA AHVPLMAAFL NAQSIEEISA ALQAWVAMHD AQVPAVKAAL AGATAPVAQA VLAFADGHAA LNPQMAALAA TDPVAAIQLH RDNLSVHDVA WDALDAAAA
C02	design_17	158	MSRAELDAYL AALEAIHQAQ IAAYKANPPK SKAEALALVD AHNAAHVALL TAFMAANPAL KAQYGDDYTA AAVGIFTEAA RAGFAWAGYH LANFAEFHPN IYDPALTDAE VIAGVNAFFA GHDWLIGNKA AVEAALPPEA AAAAADAAAA ATRAFLKL
C03	design_15	142	NRLADAVLAF AAAWAAMHAA VAAAAEGKDA RELFAVYRAH LAGHDALAAA IGKEFGVDPA LFQDWAALAA TAAALGLDNL AAALAAHAAN EAAWHPPLAT LEALLAAGRE DEAAALLRAF VAGHRAWYPA LAAAVAADTA RR

ID	Candidate	Length (aa)	Designed core sequence
C04	design_5	131	MSPFLLRHAA APAAHAFDVS DDAALRASLA AFLAAHTALV AATTAAEIAA NPFIAAFVAM HQAVAAALAA ALAAGDVRAA AAAMLAHADA HAGLLAALLG TLTPEEQALV AAWTAAVAPA FDALRAWLAG M
C05	design_23	165	AITTAAEAAA AAAAVAADVA AIWGAIAARD QAAALAAFQK TFPDAEPTTR AEAEAALAAA RATVGPIADP VAAVAWHFAL HRVVVPYVIR NVNTDPAGAG RLFGEMHRLV IEKSTGEARA LFEAAHGALA AAMLAGAPLD TIAAAHAAAA AAAHGGLVEA AAAAA
C06	design_18	167	DGTALAIDFL AAFLAMHRAV TAAPNTDPAA LAAAHAAGHV ALFTAVGARL GIEAEVQALL DRSEAALKAG DVAAARAAAA ALVTLLADAL LALPGLSPEV RAAIADFAGE HAGNLAMHDG FFTALSARLN KTITAANAAT LAALVDADVA AHAALVARFE PRVAALR
C07	repro_r49_p392	138	TVEQAQKFVE MHEKFIKEAE TAPPEESMKV LLGHYEGHQQ PGMQEGRDSA NKLSVKKYGV DLHRETGGHV DFVRYVAESL GLKDLSRIPP PGVPPPAELV RELMGKATPE QQKKSLDIFS KNHRKLVEVF KKLIEEEK
C08	repro_r40_p392	125	SELTAEELLK SSPWVRGHTE GHVELLKTYK SPVDWVIEEG EMHLKFLGLL PKLLPKETPE AQKYSLKFAE GHKTLGPKMV EVGKKKDIEG MTKIEQQHRD SDIHGPLQDG AREARDGVIE ELKKL
C09	repro_r24_p392	141	MLVPSPLAHR KLIEESKGKS AKEIAEMHQR PMHLEVPRGA SPFGEGHSLA HEEYGKLLGL PDVSPENMKG MSQEQVDKWL KIHQLLIDLN EKKVSVKDTE KELVKLGIPK EKAKKIAELA GKPMKPEIVK KQEEVAKQLG V
C10	repro_r12_p373	127	DDELAREFLK AHYSDFDTIH PPLETATKEQ LVKFFENHKK LVDKFLPKLE GTKTDLGKFV QQLLDMHRKI LSDGTKLTEE GMRKAYQEHN QGHVDLFGKA KPSVLDEVLK YSTNPEVTAL LKKAKKK
C11	repro_r08_p373	123	EPPVTVTGSN PAHGLFKKVK DDPKSKALID QHRQGHVDLL KSLGGTVSGD GDAGVLTLTF PSREALIKWA VDTLKMHQEF IEKSKSNPKA KEAFKPHEQL VKELEDIKDP EELAEKFLKM HFG
C12	repro_r03_p373	134	KLEKVREKVK KNADDFITTH LNNLTTWHNY NPDGSPRETG KKAVERHREM HRQEPLSWAI DPSSTVEQAN SLSDDDKIRL TTWFIVMHTE ILPEIKKEEP DFAKGHEQLV KDALDKVGAT IEEMKELQKE LESK
C13	GLA_design1_p373_PLACER1.53	137	MTEEQEKAVL DWMVKMHEKI IEEGKKVWDE LGPKAKKFIE GHTKLVEYAY KNKDDPRGVF QLHGRNFREF HPWLEDLYND TITNPVDKKL FQAHADSHPV TLEEMAPGKS IKDAMKLMEN GELVDKYLRG YAKYLGL
C14	GLA_design3_p373_PLACER1.63	129	MTEEQKKQYG EQAKKMGEGH LPLVEKFKEL LPKLPKDSTS YKIGKLFIDI HEDLMKKMVN AKDDEEAIKL AYEHAQSHRD SNLEQQIKNN KEKIKKESKE LYKLIKEHED NFDEMHPGLD EITAVVEKK
C15	GLA_design5_p373_PLACER1.67	162	LVPEPVKLTL PPKSTSAADA GRNVMQIINE HAQGHVELLK RLPQSTPLFV LTWAKMHEII FDKMYENLSI SDDDTKLDFQ GATTTFDPEA ARQDLQGLLE SSKDQLPAVQ EIIQDHLNNS SDHEKLANLK TGDTVKDAKD AFDGHVKLVQ KVKDMVKEGK LP
C16	GLA_design14_p392_PLACER1.66	151	PLTEEQVREA LLGLLLGAGV PEEEARELVD QFMGQFTRPY KPEDPSPTEL ARRFGEGHLK FVKEAKKNKW SPKEFLTRHM RMQMHISNDQ LERLKKDNPK AAKEIQTHFD GHDTTLKNYQ KTKDPQVFVD DIIAMHEKLE PKLLKAVEEA E
C17	GLA_design20_p392_PLACER1.80	122	LTKQQKADAL EDYAKMHEKL IKKYKEKPPK TKEEALKYWQ EHMDGHDQLG KKYGFKNGDD FANNLLFPNV PEHGERFDEM HPLLTSDLSK LTDEEILEKL RQFVEGHEKL LPVVKKAVEK LR
C18	big_w20_p373_PLACER1.77	148	MDLTVDEAAS ILEKFLTEHN SDPDLHTGLD VALDPSSTDE QKVEGAKKFV DNHEGLAKEW SKYVEPLRKV VDKYGVKTVA SKLSDEVLQA SRERFGMTPE QTVVFGVEAP EVHLKWIKKY KKEAKSGEES RKLLLEHAEQ HRQVMASA
C19	big_w32_p392_PLACER1.77	137	MPKLPTPEEI LAQAKPDPSL SPEDRFVQTD LQIHQLIIDF YEKNPEVPGR AIFQRHNETH VLLEKKYGLT WEDLLNNPSK LSKESLDYVK DHLDNEMEIH QFDISQPVDY SKVTQEMTDK FIEGHKKLVK KYSSLIK
C20	r01_p373	152	GPQPSVVTPK TKKVGDAVKK MSSKQQTEFV KTHLEMEGKT SLELSKKLSP QQLMDGFVNG HKGLVEAMET GKPLSTIKVP PYGIHPPPET LKGTPVEPIY QVHNDEHTRF QPIRDAAIKA IEDNKDDDPS IKQFAVWWAQ MHVGFIEKYY EK
C21	r03_p373	149	MTEEEVEKKA QELLDSIRDK IPPEDLPAVL GLLRFVVAHT YGVKVMEKLL KEGKPREALQ YHLDNPYFHP PPELQRKGEE WLAKNNPNIT KDTTHSVMHR ELMPELTRLF DAGRLDSLSE EEMKEYVKLL VEMHTKFNKD VWSWVDSLK
C22	r05_p373	147	TVVQLGLGMV RRIGMDEWED EFREKLKKVE DPAEGVLLVH NMGHDVLGVD ISRESMSDEL MKQWIDMHEK IIKWYNDNKD TIEKNTKNKK LLDQMKNFIK GHEILIKMTK GKPSSLIWKV HQLLFDDLHG KKVLTDEEIK KKVEEVL
C23	r06_p373	147	LKKVQEEMLK FMEEHGQSSW IHSSTSPEEW ARGHLELETK GLEKIVKIAD KEGLDPMKVT IIYDGKPVNV TKWGVGHLRM ILKAANGTPV SGREHNDMHV EMGLEGLSFA QDGDWDAMDG LVITKEDLKS IPEELLKKAE ELVKKLK

ID	Candidate	Length (aa)	Designed core sequence
C24	r07_p373	150	EEKLKKAKEA VRDALEEHLV KNPDMHRALD VLDEYEEKKK EGKVTEEDKK KLIEESKKFV EDHEKLVKFI KEKVKEVEKI SKEVELPEDV KKTLKALKRL VKVHTEMIEK MKKAPDDAEV RAKLLQEHRD SHSPEDEQTL LDSLKKLSKL
C25	r10_p392	148	MKEEMQKELD QMPEYPKSEQ HNKGTTTSKS IDDVKGFMDM HEKLLSKKLT PREFFLEHAR MLPKDVREQV LGMMEKAEKA GLLEDVVNLW RKMHEKIIKK FKEVEKKKPN DEKAFQKIVD EHNQGHVRLF KALDKAIENK EPLKDSVL
C26	r13_p392	148	KVKEAVEKVK KLWEETDLSS NELHDETEPV MHRYDRDEEG LKVFLAGHDT LNKLSLENKE PLTGLWPSLE QLKAASGEAA DRILAGEDPM DAHNLSHTGK SDPNYKPSKE AQKIMDEAEK TMEKNGVKLT KDNGMTFMHL VIGKATKK
C27	r18_p392	136	KLSKIDLEDS VKVAQKILDA GLPELKKAVG KLDEKGLKEL RKFLDGHREL VKWYKDTPGI TGEQFGQIHT DSGEIHGVLG SPDQKVRDAF RVHADMHDEL IKLGVITEKP DGTIVMSPAA VKMHEMFIKQ VEPLLP
C28	r21_p392	164	FEEVVKSFVY LHLKLRDKMP PLMAESHQPI VDTLKELLGE PKETFPFKGK DHNSSHVDLM ESLVKTLGVD NPATEAVGIL GVVNPETAKY VSERGKEIFK KIKGKTIDEA EKIILEETDL PKEVATLIAV HMAGMVHTDL GLKGGDSLEQ GKENMVRRLR ETFS
C29	r22_p392	159	KKEKIQKIVD SLPEPKDGSK ETDPDKLMRL ALRHYLLFDE MHVSPEELQT LLYVKKDPET AKEKVRNFFV GHANELLNDP KLAKELDEAI KKSKDPELLL KKVQEHYDGH TPEITQAFDN IVKKALEKKP VTDEDVQLVR DELQMHLEDS KKTLKDLKK
C30	r24_p392	159	TEKKLQEVVD SLPLPKDGSK ETDKKQLMRL ALLHRLLFDE WHVSPETLKK LLEKDKDNEK LKELVRNFFV GHANELLNDP KLGEELKKAI EESKDPKLLL KLVQDHYDSH TPEIEQAFDN IVEKALNKEE VTDEDAKLVQ KYMQMHQKDV EKTVKTLKK
C31	r26_p392	136	SKMKKLLDQH DENRDEMHNP EGKDDKDRLK KSGLAHEKLV LDMVKNAWDD KIKGKELLKW FDEVAFTFPT PVFKDPKIKK LWNDHNDGHV TLRKKLKANP DKEINGKEIF QMHLDWLKKL EDEKVITLSP EVKKSI
C32	r27_p392	151	PTLEEVIESS LKGVESWLEH ERAHEGLEDL RKKTSVEDKM KYGKAMLEMH QTLEPKALKN FQEAVKKSEP LKDTPTGKRI YTSMTKGKQA AQDHLDKVNP LLEKAIKTET LIDTDPDKVI EEIDKFLQEH DGALHAEVQP LYEYLKKLKK K
C33	r28_p392	161	MTLEETLKKA REMGLDLTIG GHGNIVKKAK ESKDESAIKL LDAHNAMHVA MLDYLKNPND EKKKKKFIEK IDEAIKVSLE SKESPALKLF RKVHGDLLDG TDEKDFIETH LALEVDAPDF KSLSPEQQEL WIQLPRLMHT IVGSKDEKLR QKAKEELLKL L

Note: sequences are shown without expression tags. The six Batch 1 constructs carried a C-terminal GSGSHHHHHH tag. Expression-tag information is reported only where it was documented in the experimental record; all other entries list the designed core sequences. These results show that the selected candidates reproduced the prescribed dicopper-pocket geometry in the computational models. They do not by themselves establish folding, copper binding, or catalytic function; those conclusions require expression, metal-binding, and enzymatic experiments.

Expression, Purification, and Candidate Screening

All recombinant expression plasmids were synthesized by GenScript using pET-28a as the vector backbone. The designed-protein constructs and the non-Cu protein control contained a C-terminal thrombin recognition sequence followed by a 6×His tag. The HC4 expression construct was prepared in pET-28a with an N-terminal 6×His tag followed by a Tobacco Etch Virus (TEV) protease cleavage site, as reported previously (Eng et al., 2026). The non-Cu protein control was the previously designed GZMK-binding protein 9-102.

The plasmids were transformed into chemically competent Escherichia coli BL21(DE3) cells (Vazyme, cat. no. C504-03) and plated on LB agar containing 50 μg mL^{-1} kanamycin. After overnight incubation at 37 ° C, individual colonies were inoculated into 5 mL of LB medium containing 50 μg mL^{-1} kanamycin and cultured at 37 ° C for 16 h. The overnight cultures were subsequently used to inoculate 500 mL of LB medium containing the same concentration of kanamycin. Cultures were grown at 37 °C for 5 h, shifted to 18 °C, and induced with 0.5 mM isopropyl β-D-1-thiogalactopyranoside (IPTG) for 24 h before the cells were harvested by centrifugation.

Cell pellets were resuspended in buffer A (50 mM Tris, 300 mM NaCl, pH 8.0) and lysed by high-pressure homogenization. Following centrifugation, the clarified lysates were batch-incubated with Ni Sepharose FF (NTA) resin (Vazyme, cat. no. HP202-02). The resin was washed with buffer A supplemented with 20 mM imidazole, and bound proteins were eluted with buffer A supplemented with 250 mM imidazole.

The eluates were buffer-exchanged into buffer A using 15-mL Amicon Ultra centrifugal filter units with a 10-kDa molecular-weight cutoff (Merck Millipore, cat. no. UFC901024) to remove imidazole. The C-terminal His tags of the designed proteins and protein 9-102 were removed by overnight thrombin digestion at 4 °C. The N-terminal His tag of HC4 was removed using laboratory-prepared TEV protease under the same temperature and incubation conditions. Following cleavage, the samples were reapplied to Ni Sepharose FF (NTA) resin, and the flow-through fractions containing the cleaved proteins were collected. EDTA was then added to a final concentration of 3 mM, and the samples were incubated for 30 min before buffer exchange into buffer A to remove EDTA and residual nickel ions.

A portion of each protein preparation was retained as the unloaded sample. To prepare Cu-loaded samples, $CuSO_4$ was added to a final concentration of 400 μM, and the proteins were incubated at 4 ° C for 2 h. Unbound copper was subsequently removed by buffer exchange into buffer A. All buffer-exchange steps were performed using buffer A. Protein concentrations were determined from absorbance at 280 nm.

Among the experimentally screened candidates, Design 15 and Design 17 showed the most promising L-DOPA oxidation activity and were therefore advanced to subsequent analyses of copper dependence, substrate selectivity, and apparent kinetics.

Experimental Validation

L-DOPA activity screening has been completed for 12 candidates. Design 15 and Design 17 showed detectable activity, whereas the other ten candidates showed no detectable activity under the same assay conditions. Because the remaining 21 candidates have not

yet completed expression and activity testing under equivalent conditions, an overall experimental hit rate for all 33 candidates is not calculated. The complete available enzymology data for Design 15 and Design 17 are presented in Figure C3 and Tables S4–S7.

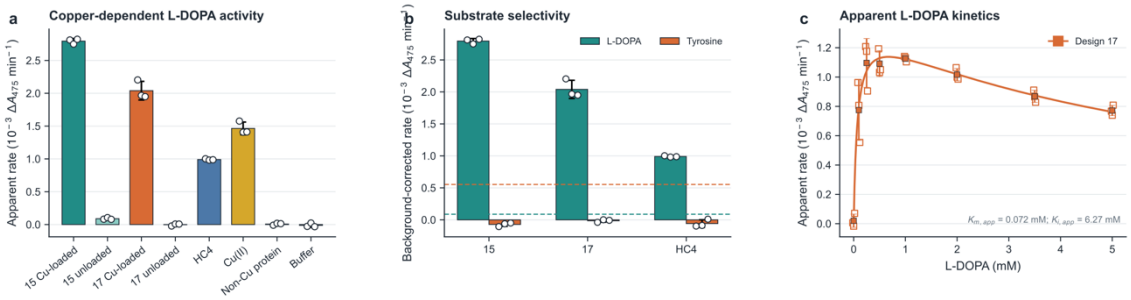


Figure C3. Experimental validation of Design 15 and Design 17. (a) Copper-dependent L-DOPA oxidation activity with protein and buffer controls. (b) Background-corrected responses to L-DOPA and tyrosine; dashed lines denote 3 SD of the corresponding enzyme-free blank distribution. (c) Apparent L-DOPA kinetics of Design 17 fitted with a substrate-inhibition model. Open symbols represent technical wells; bars and error bars show mean ± SD.

L-DOPA Activity and Tyrosine Selectivity

Activity and selectivity data were collected at 475 nm using a Tecan Spark microplate reader. The program comprised 25 kinetic cycles, with 5 s of linear shaking before each cycle and a 2 min interval between cycles; 25 time points per well covered 0-55.60 min. A linear regression was fitted to the A475-time trace of each well. L-DOPA conditions were corrected by subtracting the mean slope of eight enzyme-free L-DOPA blanks, and tyrosine conditions by subtracting the mean slope of 12 enzyme-free tyrosine blanks. Each protein-substrate condition contained three technical wells. A detectable response was operationally defined as a background-corrected rate exceeding 3 SD of the corresponding blank distribution.

The apparent L-DOPA rates of Cu-loaded Design 15 and Design 17 were (2.795 ± 0.039) × 10^{-3} and (2.040 ± 0.142) × 10^{-3} ΔA475 min^{-1}, respectively, whereas the unloaded proteins remained near background (Figure C3a; Table S4). The L-DOPA responses of both designed proteins exceeded the corresponding 3-SD blank criterion, while their tyrosine responses did not (Figure C3b; Table S5). These results support copper-dependent L-DOPA oxidation and show that neither Design 15 nor Design 17 had detectable tyrosine activity in this assay.

Table S4. Complete technical-well data for L-DOPA activity and controls. Values are background-corrected apparent rates in 10^{-3} ΔA475 min^{-1}.

Condition	Replicate 1	Replicate 2	Replicate 3	Mean ± SD	n
Design 15, Cu-loaded	2.812	2.750	2.823	2.795 ± 0.039	3
Design 15, unloaded	0.082	0.105	0.080	0.089 ± 0.014	3
Design 17, Cu-loaded	2.203	1.967	1.949	2.040 ± 0.142	3
Design 17, unloaded	-0.022	0.008	0.007	-0.002 ± 0.017	3
HC4	1.002	0.982	0.987	0.990 ± 0.010	3

Condition	Replicate 1	Replicate 2	Replicate 3	Mean ± SD	n
Free Cu(II)	1.576	1.407	1.411	1.465 ± 0.097	3
Non-Cu protein control	-0.010	0.019	0.013	0.007 ± 0.015	3
Buffer	-0.028	0.023	-0.032	-0.012 ± 0.031	3

Table S5. Complete technical-well data for L-DOPA/tyrosine selectivity. Values are background-corrected apparent rates in 10^{-3} ΔA475 min^{-1}. "Relative to blank + 3 SD" compares each condition mean with the operational threshold of 3 SD above the background-corrected zero level.

Protein	Substrate	Replicate 1	Replicate 2	Replicate 3	Mean ± SD	Relative to blank + 3 SD	n
Design 15	L-DOPA	2.812	2.750	2.823	2.795 ± 0.039	Above	3
Design 15	tyrosine	-0.106	-0.062	-0.049	-0.072 ± 0.030	Below	3
Design 17	L-DOPA	2.203	1.967	1.949	2.040 ± 0.142	Above	3
Design 17	tyrosine	-0.039	0.001	-0.007	-0.015 ± 0.021	Below	3
HC4	L-DOPA	1.002	0.982	0.987	0.990 ± 0.010	Above	3
HC4	tyrosine	-0.098	-0.088	0.010	-0.058 ± 0.060	Below	3

The Cu-dependence and substrate-selectivity assays were performed in transparent, flat-bottom 96-well plates with a total reaction volume of 200 µL per well. All proteins were added from 3 mg mL^{-1} solutions. Each protein-containing well comprised 160 µL of 1× PBS, 20 µL of protein solution, and 20 µL of substrate solution, giving a final protein concentration of 0.30 mg mL^{-1} . L-DOPA was added from a 10 mM stock solution prepared in 1× PBS to a final concentration of 1.0 mM. L-Tyrosine was tested at the same final concentration. Before substrate addition, the mixtures containing protein and PBS were equilibrated at 37 °C for 3-5 min.

The Cu-dependence experiment compared Cu-loaded and unloaded Design 15 and Design 17. HC4, free Cu(II), the non-Cu protein control, and buffer-only wells were included as controls. HC4 and the non-Cu protein control, identified as the GZMK-binding protein 9-102, were tested at the same final protein concentration. The free-Cu(II) control contained $CuSO_4$ at a final concentration of 400 µM without protein. No additional free Cu(II) was added to reactions containing Cu-loaded proteins after buffer exchange.

For the substrate-selectivity comparison, Design 15, Design 17, and HC4 were tested separately with L-DOPA or L-tyrosine, together with the corresponding enzyme-free substrate blanks. Each protein–substrate condition contained three technical wells.

Apparent L-DOPA Kinetics

Kinetic reactions had a total volume of 200 µL and a final protein concentration of 10 µM; A475 was recorded at 37 °C. Design 15 and Design 17 were loaded with Cu(II) and buffer-

exchanged before the assay, with no additional free Cu(II) added to the reaction. Final L-DOPA concentrations were 0, 0.10, 0.25, 0.50, 1.00, 2.00, 3.50, and 5.00 mM. Each protein-concentration condition contained three technical wells and three enzyme-free blanks at the same substrate concentration. The predefined analysis window was 120-360 s for all wells; the instrument time points falling within this interval were 149.246, 186.604, 223.926, 261.271, 298.601, and 335.846 s. A linear regression was fitted to A475 versus time for each well and corrected using the mean blank slope at the corresponding substrate concentration.

All background-corrected technical-well slopes were fitted by nonlinear least squares using SciPy curve_fit (Virtanen et al., 2020). For Design 15, the Michaelis–Menten model yielded Km,app = 0.078 mM and Vmax,app = 1.574 × 10^{-3} ΔA475 min^{-1}. Design 17 showed lower rates at higher substrate concentrations; the substrate-inhibition model had a lower AIC than the simple Michaelis–Menten model and yielded Km,app = 0.072 mM, Vmax,app = 1.381× 10^{-3} ΔA475 min^{-1}, and Ki,app = 6.27 mM (Figure C3c; Table S6). This model comparison describes the current dataset and does not independently establish a catalytic inhibition mechanism for Design 17.

Table S6. Apparent kinetic fits for Design 15 and Design 17. Design 15 follows the Michaelis–Menten fit reported in the main text. For Design 17, the preferred model was selected by the lower AIC. Vmax,app is reported in 10^{-3} ΔA475 min^{-1}; SE denotes the standard error obtained from the covariance matrix of the nonlinear fit.

Protein	Model	Vmax,app ± SE	Km,app ± SE (mM)	Ki,app ± SE (mM)	R^2	AIC	Preferred
Design 15	Michaelis–Menten	1.574	0.078	NA	0.933	NA	Yes
Design 17	Michaelis–Menten	0.997 ± 0.046	0.014 ± 0.014	NA	0.805	-417.2	No
Design 17	Substrate inhibition	1.381 ± 0.090	0.072 ± 0.019	6.27 ± 1.43	0.937	-442.1	Yes

Table S7. Complete background-corrected rates at each L-DOPA concentration. Replicate values and mean ± SD are reported in 10^{-3} ΔA475 min^{-1}; each value represents one technical well.

L-DOPA (mM)	Design 15 replicates	Design 15 mean ± SD	Design 17 replicates	Design 17 mean ± SD
0.00	0.025, 0.025, -0.026	0.008 ± 0.029	0.006, -0.017, 0.070	0.020 ± 0.045
0.10	1.307, 1.046, 0.375	0.909 ± 0.481	0.963, 0.807, 0.554	0.775 ± 0.206
0.25	1.653, 1.167, 0.818	1.213 ± 0.420	1.208, 1.176, 0.905	1.096 ± 0.167
0.50	1.643, 1.275, 1.138	1.352 ± 0.261	1.193, 1.032, 1.050	1.092 ± 0.088
1.00	1.779, 1.430, 1.274	1.494 ± 0.259	1.141, 1.131, 1.104	1.125 ± 0.019
2.00	1.826, 1.413, 1.353	1.531 ± 0.258	1.064, 1.000, 0.986	1.017 ± 0.042
3.50	2.114, 1.352, 1.283	1.583 ± 0.461	0.911, 0.865, 0.828	0.868 ± 0.041
5.00	1.571, 1.332, 1.369	1.424 ± 0.129	0.767, 0.740, 0.808	0.772 ± 0.035

Because the effective optical path length and extinction coefficient of dopaquinone have not been established for this plate format and assay condition, all rates and Vmax values are reported in ΔA475 min^{-1} rather than converted to molar rates, and kcat is not calculated. Here, n = 3 denotes technical wells on the same plate rather than independent experiments or independent protein preparations; independent replication remains necessary for journal-level statistical inference.

Code and Data Availability

Design and analysis code is available at https://github.com/Terry-Wang-Lynx/ppo-design. The raw natural-PPO screening record is reproduced in Table S1; candidate structural metrics and designed core sequences are provided in Tables S2 and S3. The enzymology results can be audited against the processed machine-readable results and the original activity/selectivity and kinetic workbooks; the predefined kinetic workflow is retained in the original protocol.

Scope and Limitations

Computational filtering measures agreement with predefined geometric conditions and is not equivalent to protein solubility, copper occupancy, catalytic rate, or substrate selectivity. Sampling and post-processing rules evolved between design rounds; Figure C2 therefore compares the five core geometric metrics that could be recalculated uniformly for all 33 candidates. An experimental hit rate should be calculated only after expression and activity status has been completed for every candidate and should not be extrapolated from the current partial dataset.

No catalytic response has been detected after electrode immobilization so far. The cause remains unresolved, and activity loss during glutaraldehyde cross-linking is currently being investigated as a possible explanation.

D. Exploratory SBP-Based Electrochemical Sensing

Computational Design of L-DOPA-Binding SBPs

The tryptophan-bound solute-binding protein structure 3LFT was selected as the starting scaffold to exploit its ligand-induced hinge motion. To redesign the binding pocket for L-DOPA while preserving the open-to-closed 'Venus flytrap' transition, we constructed a computational sequence-design pipeline with reinforcement learning.
LigandMPNN was fine-tuned under a Group Relative Policy Optimization (GRPO) framework to generate sequences in the target ligand-containing context (Dauparas et al., 2025; Shao et al., 2024). Hallucination-based design was also explored to expand the backbone conformational space around the binding pocket. Candidate trajectories were evaluated with AlphaFold 3 using ipTM, pTM, PAE, and RMSD-based rewards (Abramson et al., 2024). Tryptophan and tyrosine were introduced as decoys, and sequences predicted to close around either decoy were penalized to bias the design toward L-DOPA recognition. Candidates passing the computational filters were advanced to experimental evaluation.

Electrochemical Characterization and Dual-Frequency KDM Correction

Redox-reporter-modified proteins were oriented on gold electrodes through NTA–Cu(II)–His affinity chemistry (Zhu et al., 2023), and ligand-dependent responses were measured by square-wave voltammetry (SWV). Sequential peak-current measurements at protein modification concentrations of 0.2, 1, and 3 µM showed progressive baseline loss during increasing and decreasing L-Trp steps (Figure D1).

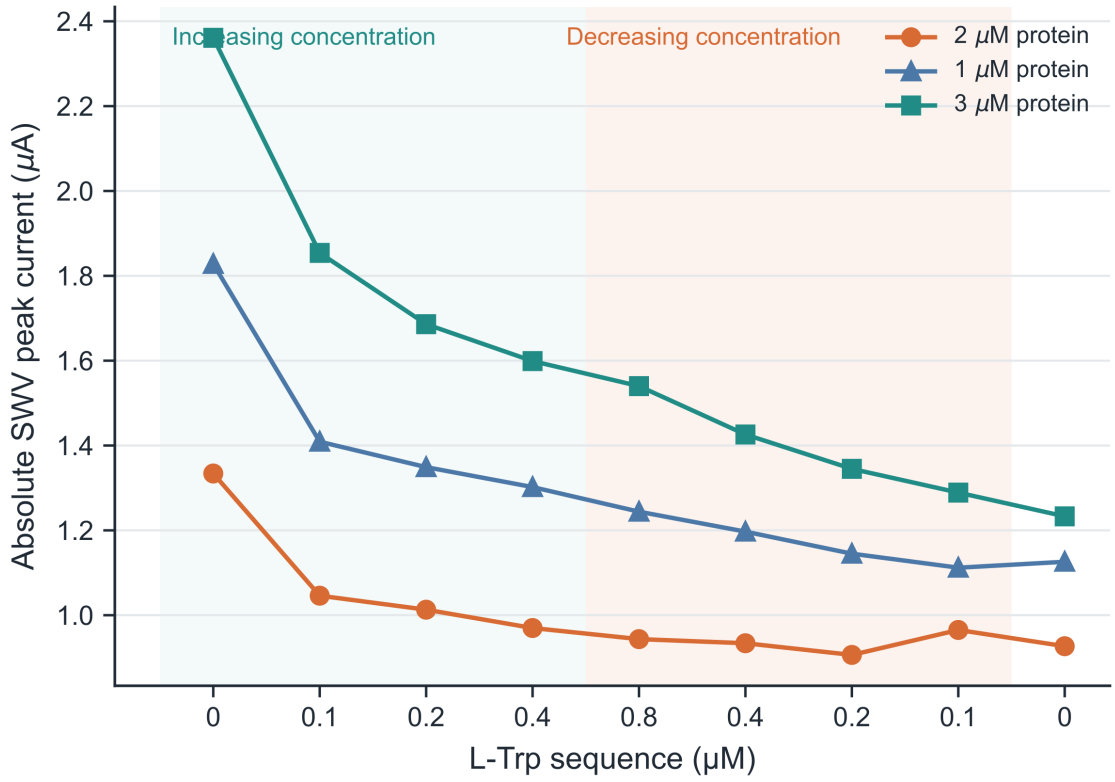


Figure D1. Sequential SWV peak-current responses during increasing and decreasing L-Trp concentrations at three protein modification concentrations.

The raw response showed pronounced baseline drift, consistent with loss of electroactive surface coverage or other interfacial drift. To separate ligand-dependent changes from proportional baseline loss, we applied kinetic differential measurements (KDM) (Arroyo-Currás et al., 2017).

KDM exploits the frequency dependence of conformational electrochemical signaling. Loss of surface-bound redox reporters decreases the total electroactive probe population and therefore affects signals at both interrogation frequencies. By contrast, a ligand-induced conformational change alters electron-transfer kinetics, making its signal contribution frequency dependent.

The two frequency traces were aligned at the initial state using $\alpha = I_{10\ Hz}(0)/I_{100\ Hz}(0)$, and the differential signal was calculated as $I_KDM(t) = I_{10\ Hz}(t) - \alpha \times I_{100\ Hz}(t)$. Under this treatment, the scaled 100 Hz trace served as a drift reference, and subtraction reduced the common baseline component (Figure D2).

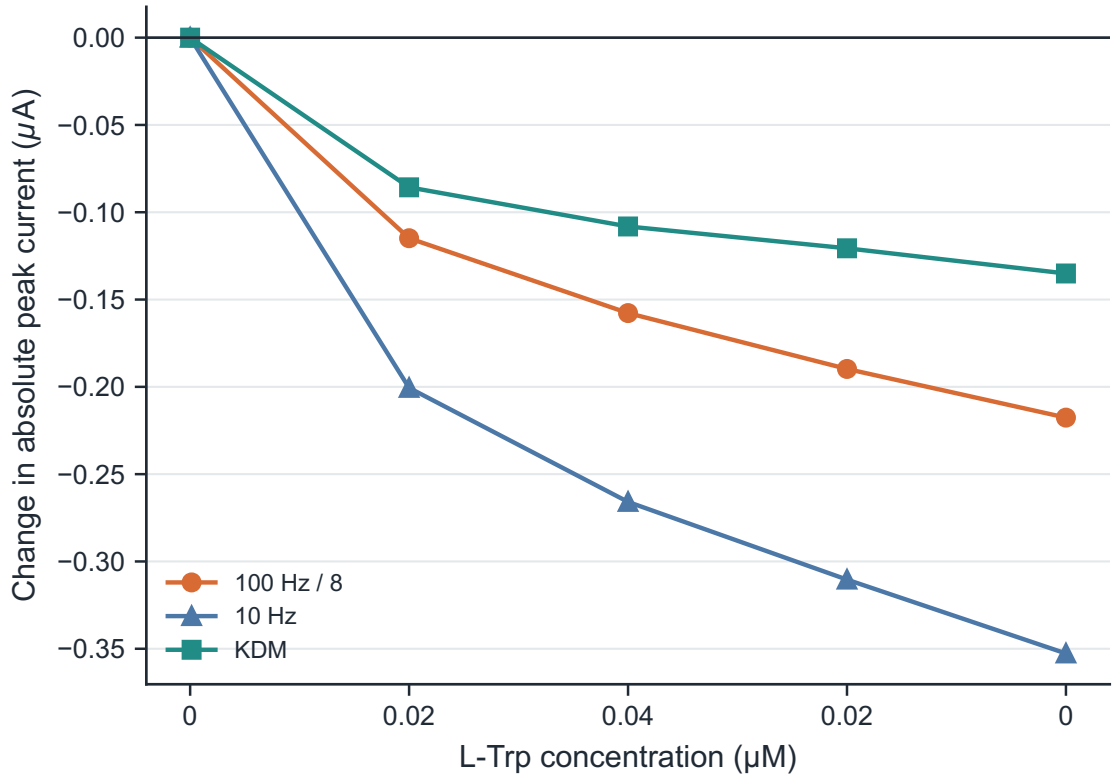


Figure D2. Dual-frequency KDM correction of the sequential L-Trp response. The 10 Hz trace, scaled 100 Hz reference, and resulting KDM signal are shown.

However, the sensor response remained irreversible. The same non-recovering response was observed across a broad range of protein modification concentrations, suggesting that surface crowding alone may not explain the behavior. The underlying mechanism remains unresolved. We currently hypothesize that site-specific anchoring may orient the SBP unfavorably relative to the electrode and thereby limit ligand dissociation after

conformational closure. Further experiments are required to test this hypothesis and establish a reversible response.

E. Wearable Readout Hardware: Configuration and Measured Performance

This appendix holds the electrical detail removed from Section 2.4 and the full measured performance of the front end summarised in Table 1.

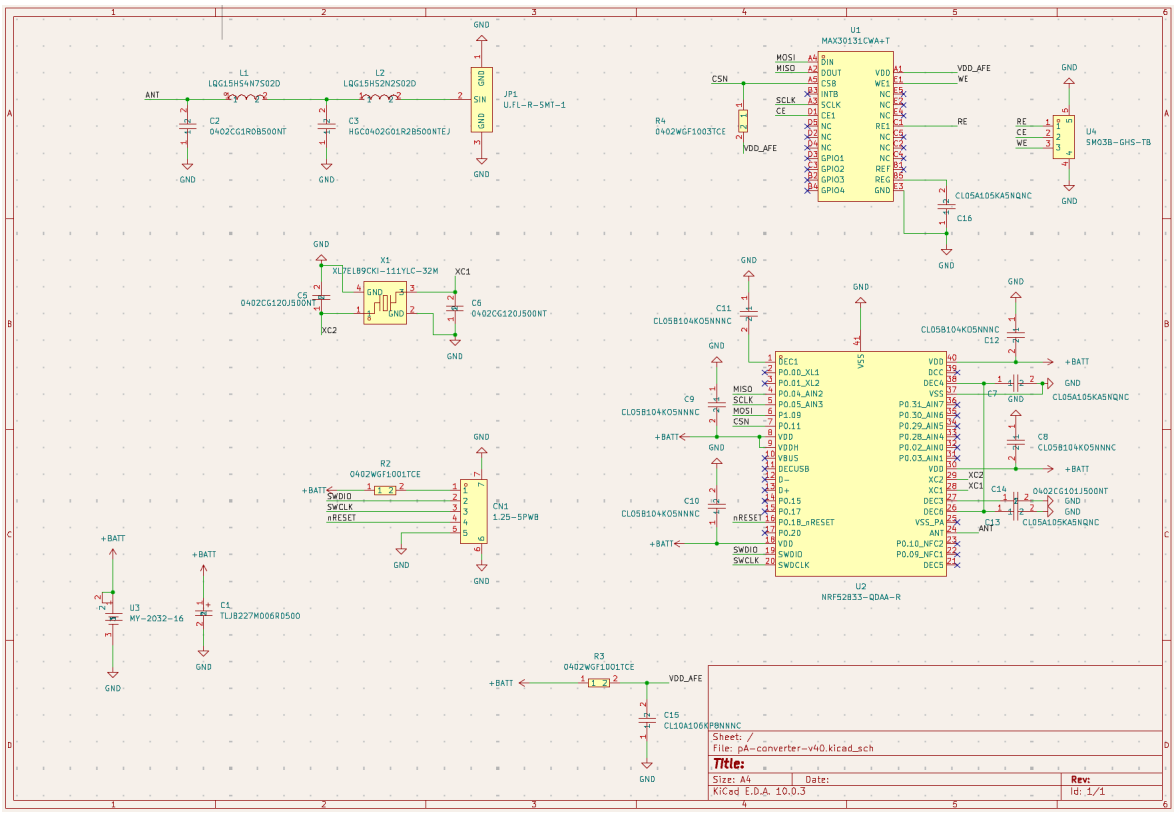


Figure E1. Electrical schematic of the wearable electrochemical readout, including the MAX30131 electrochemical front end, nRF52833 Bluetooth controller, power filtering, antenna, battery input, and electrode/debug connectors.

E.1 Electrical Configuration

The electrode array connects through a three-way 1.25 mm latching connector carrying the working, reference and counter electrode; a separate five-way connector carries the serial-wire debug link and is used for programming. The radio drives a u.FL connector and an external pre-matched flex antenna, so no antenna tuning is required.

The coin cell feeds both devices through a 220 µF tantalum reservoir, which absorbs the millisecond-scale current step of a radio transmission, and the front-end supply is further separated from the digital rail by a 1 kΩ and 10 µF network so that switching activity in the controller cannot reach the measurement reference.

The cell is held at a potential generated as the difference of two independently programmed 12-bit DAC outputs referred to the internal 1.536 V reference, giving a 0.375 mV setpoint step. The current channel offers six full-scale ranges from 50 nA to 2 µA, each with a selectable internal offset current that sets how far the measurement extends in the

reduction direction. Conversion time and sampling period are independently programmable, so resolution can be traded against bandwidth: the analyte response is a slowly varying steady-state current, and lengthening the integration window is the most direct way to obtain resolution.

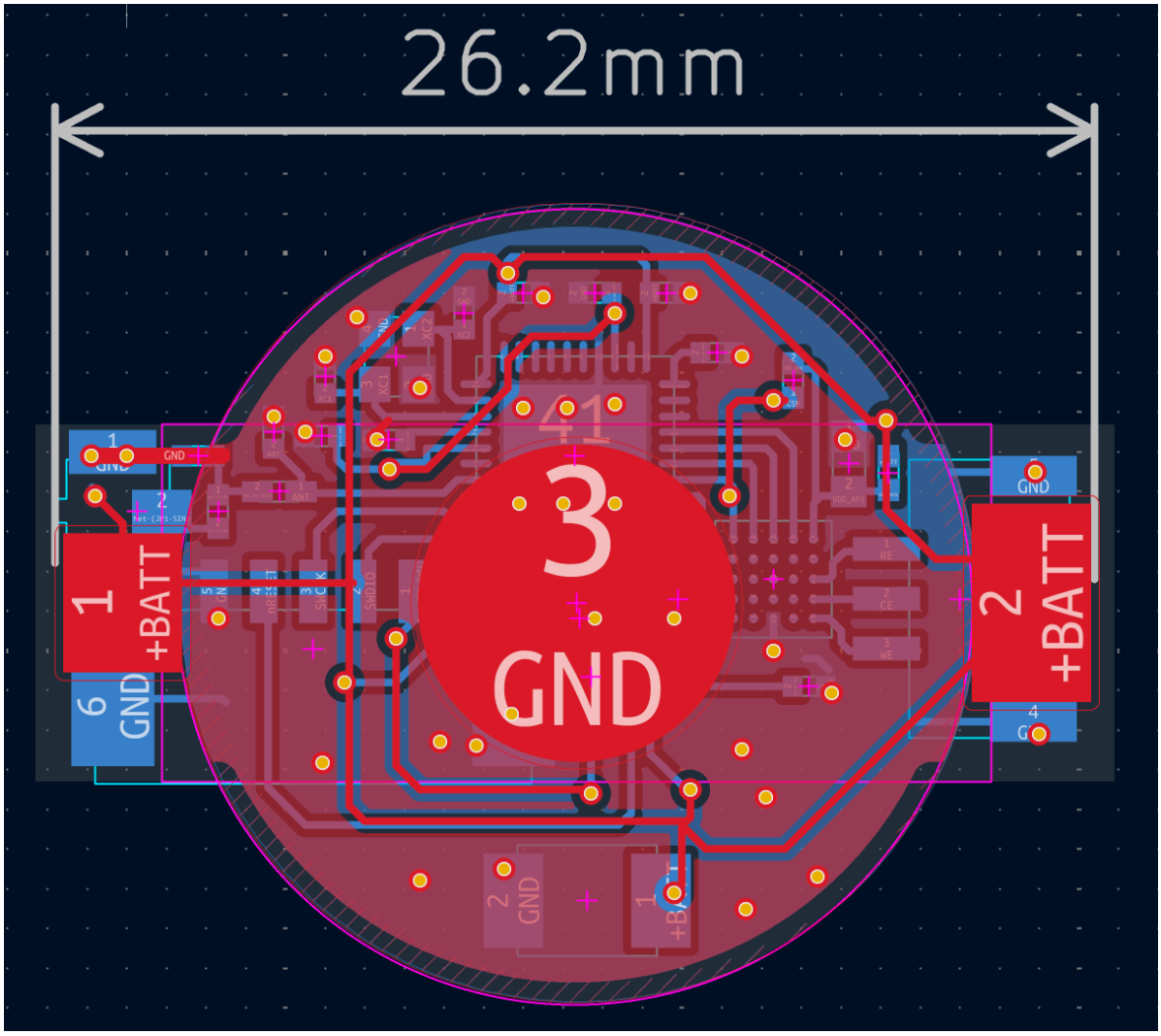


Figure E2. Printed-circuit-board layout and mechanical outline of the coin-sized wearable electrochemical readout.

E.2 Measured Performance

Table E1. Configuration and measured performance of the wearable readout.

Parameter	Value	Condition or source
Physical		
Board outline	27.20 × 20.04 mm, 386 mm²	two copper layers, 27 placed components
Active devices	2	integrated electrochemical front end + Bluetooth controller
Power-management ICs	0	coin cell connected directly to both devices

Parameter	Value	Condition or source
Coin cell holder	188 mm², 49 % of board area	courtyard area
Both integrated circuits	34 mm², under a tenth of the board	courtyard area
Potential control		
Setpoint resolution	0.375 mV	12-bit DAC on the 1.536 V internal reference
Configured potential window	−0.6 to +0.6 V vs Ag/AgCl	difference of two DAC outputs
Reference temperature drift	30 ppm °C^{-1}	device specification
Current measurement		
Full-scale ranges	50, 100, 250, 500, 1000, 2000 nA	selectable at run time
Quantisation step	0.763 pA (50 nA range) to 30.5 pA (2 µA range)	16-bit conversion
Conversion time	31 ms to 476 ms	programmable; sets 12-bit to 16-bit resolution
Sampling period	0.124 s to 3.76 s	programmable, independent of conversion time
On-chip result buffer	256 samples	≈32 s at the shortest sampling period
Measured noise and stability		
Noise, σ / 3σ	1.71 pA / 5.12 pA	electrode port open; 50 nA range, 1.88 s integration, 5.5 min
Noise-free resolution	12.7 bit	as above
Minimum Allan deviation	0.945 pA at τ = 18.8 s	as above; white-noise to drift crossover
Noise, σ, on a connected electrode	0.62 nA	screen-printed electrode in 50 µM L-DOPA at +0.2 V; 2 µA range, 31 ms integration, WE series resistor engaged, final 20 s
Largest sample-to-sample step	0.98 nA	as above, after the first 10 s
Electrode thermal-noise floor, 3σ	0.18 pA	computed from the measured impedance spectrum by the fluctuation–dissipation relation; contains no instrument parameter
System		
Operating temperature	0 to 70 °C	commercial temperature grade of the front end

Parameter	Value	Condition or source
Firmware footprint	56 kB flash, 11.6 kB RAM	of 512 kB and 128 kB available

E.3 Conditions Attached to the On-Electrode Figure

The on-electrode noise in Table E1 was taken on a screen-printed electrode at +0.2 V with the 2 µA range selected, a configuration chosen for a steady current about a hundred times larger than the microneedle produces at −0.2 V. On that range the quantisation step is 30.5 pA, so the figure is a bound on the readout in that configuration rather than the resolution available to the microneedle measurement, for which the 50 nA range applies. Engaging the working-electrode series resistor, which stabilises the amplifier against the large double-layer capacitance of these electrodes, reduced the noise on that record from 3.5 nA to 0.62 nA and removed the step transitions present without it.

Three quantities are not yet measured and are stated as such: the noise on the microneedle array at −0.2 V with the range matched to its signal; drift over records longer than two hours, for which the present −96 pA h^{-1} figure is dominated by warm-up; and the linearity of the front end against an externally injected known current.

F. Microfluidic Module and Sample Injection System

Modular Multilayer PDMS Microchamber Platform

A modular microfluidic platform was developed to accommodate planar, microneedle, and combined electrode configurations. The device was fabricated from pre-cured polydimethylsiloxane (PDMS) components and used a mechanically compressed, reversibly assembled structure instead of permanent PDMS–electrode bonding. This improved compatibility with electrodes of different geometries and allowed the sensing elements to be replaced when required.

The cartridge consisted of upper and lower PDMS support layers, one or more pre-cured PDMS chamber spacers, and two rigid polymer clamping plates. The support layers provided compliant sealing interfaces, while the central spacer defined the sensing area, chamber thickness, and working volume. Torque-controlled threaded fasteners distributed compression and improved sealing and chamber-volume reproducibility. The chamber-facing PDMS surfaces were treated to achieve wettability comparable to that of the electrode surfaces, promoting uniform filling and reducing bubble entrapment.

Samples were transported through polyethylene tubing with an inner diameter of 0.10 mm. The inlet and outlet were positioned on opposite sides of the chamber, and the outlet was connected to a microinjection pump operated in withdrawal mode to generate slight negative pressure.

Planar-Electrode Cartridge

For planar and screen-printed electrodes, a pre-cured PDMS spacer containing a 10 mm circular opening was positioned between the support layers. The target chamber volume was approximately 50 µL, providing sufficient coverage of the active electrode area while retaining tolerance for minor variations in electrode positioning, spacer alignment, and assembly compression.

A 10 mm-diameter cylindrical chamber with a volume of 50 µL requires a theoretical thickness of approximately 0.64 mm. To compensate for compression during clamping, the spacer was fabricated with an uncompressed thickness of approximately 0.74 mm. The electrode was aligned with the circular opening so that the active region remained exposed to the liquid phase. Upper and lower PDMS support layers, each 5.0 mm thick, helped distribute the applied load and maintain the chamber geometry. The non-permanently bonded structure also allowed convenient replacement of screen-printed electrodes.

Microneedle-Electrode Cartridge

The microneedle cartridge used two pre-cured PDMS spacers, each 0.25 mm thick, with the microneedle electrode positioned between them. This configuration provided fluidic access to both sides of the electrode and prevented either side from being blocked by a solid support, facilitating wetting and reducing differences in mass transport.

The total nominal chamber thickness was 0.50 mm. For a 10 mm-diameter opening, the geometric volume was approximately 39 µL before accounting for electrode displacement. The cartridge retained the same support layers, clamping structure, tubing connections, surface treatment, and negative-pressure operation used for the planar-electrode design.

Hybrid Microneedle–Planar Electrode Cartridge

A dual-electrode cartridge was developed to integrate a microneedle electrode and a planar electrode within the same fluidic module. Two pre-cured PDMS spacers with thicknesses of 0.20 and 0.30 mm were used. The microneedle electrode was positioned between the spacers, while the planar electrode was placed on the outer side of the thicker spacer.

The asymmetric spacing increased the separation between the sensing elements and was designed to reduce electric-field coupling and electrochemical cross-talk. The working surfaces were oriented in the same direction rather than facing each other, further minimizing direct electrode-to-electrode interaction. Both electrodes remained exposed to the same continuously exchanged sample. The total nominal spacer thickness was 0.50 mm, corresponding to an initial chamber volume of approximately 39 µL before electrode displacement.

Fabrication of Pre-Cured PDMS Spacers

PDMS base prepolymer and curing agent were mixed at a mass ratio of 10:1 and degassed under vacuum until no visible bubbles remained. A thickness-controlled mold was assembled from two rigid polymer plates and a pre-cut U-shaped silicone sheet whose thickness matched the desired spacer thickness.

The degassed PDMS mixture was introduced into the mold using a syringe and cured at 65 °C for 30 min. After cooling, the mold was disassembled and the pre-cured PDMS sheet was removed. A 10 mm sensing opening was formed using a manual biopsy punch, and smaller inlet and outlet ports were made using manual punches matched to the tubing dimensions. The prepared spacer was then aligned with the selected electrode and assembled between the PDMS support layers and rigid clamping plates.

Sample Injection and Replacement

The cartridge was connected to a 150 µL sample reservoir with an upper-wide and lower-narrow geometry. This reduced the contact area between successive samples and allowed the next sample to be added shortly before depletion of the previous one. At the outlet, the microinjection pump withdrew liquid at 100 µL/min.

Approximately 50 µL was used for the planar-electrode cartridge, whereas approximately 40 µL was used for the microneedle and hybrid cartridges. During each measurement cycle, one chamber volume was first withdrawn for rinsing, followed by a second chamber volume for electrochemical measurement. When required, withdrawal at 300 µL/min for 5 s was used to remove residual liquid or trapped air from the tubing. The low chamber volume, matched surface wettability, negative-pressure operation, and mechanically stabilized structure supported reproducible sample handling across the different electrode configurations.

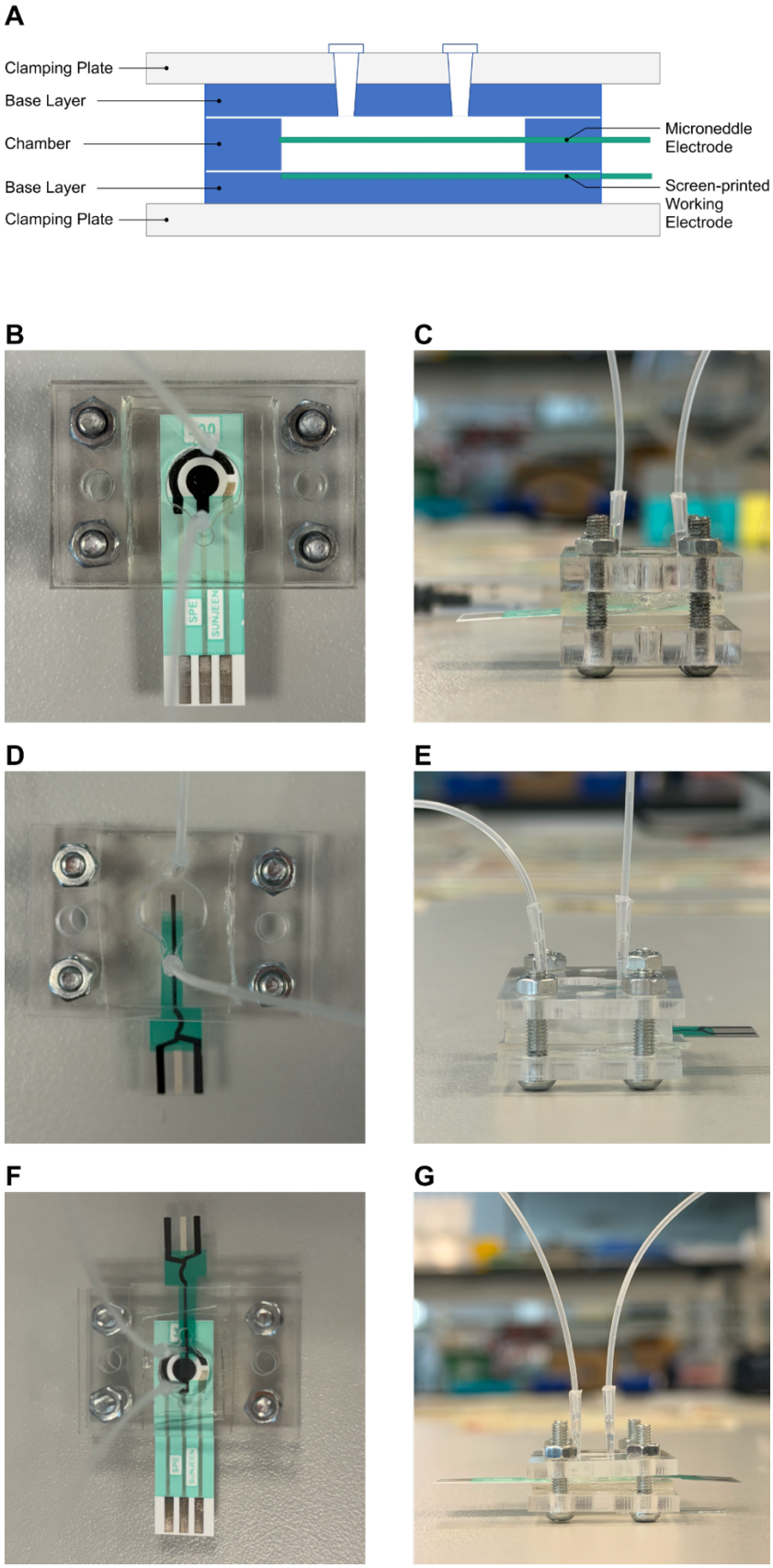


Figure F1. Modular PDMS chambers for different electrode configurations.
(a, b) General multilayer chamber assembly. (c, d) Planar-electrode chamber with a 10 mm-diameter, approximately 50 µL sensing chamber. (e, f) Microneedle-electrode chamber formed using two 0.25 mm PDMS spacers. (g, h) Hybrid microneedle–planar electrode chamber formed using 0.20 and 0.30 mm PDMS spacers.

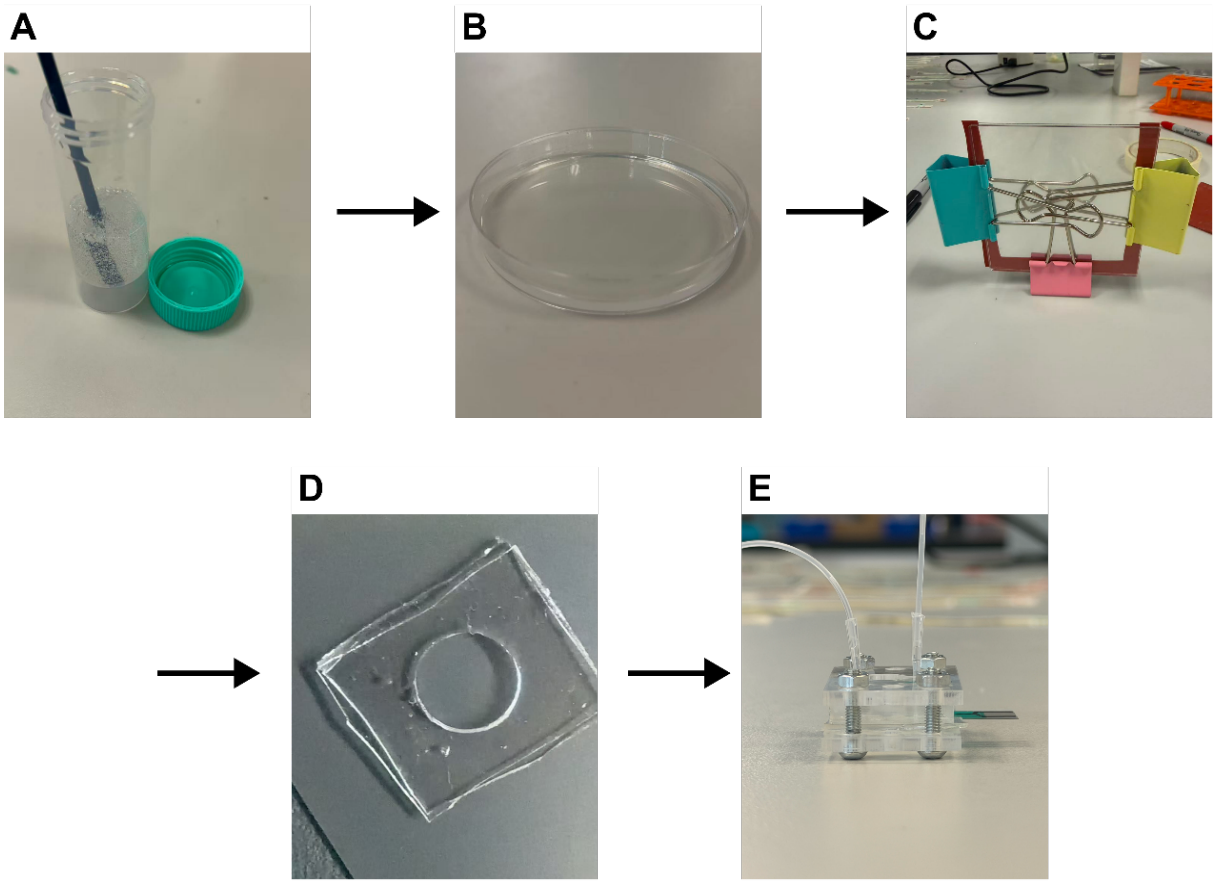


Figure F2. Fabrication of pre-cured PDMS chamber spacers.
(A) Mixing and vacuum degassing of PDMS prepolymer and curing agent. (B) Injection into a thickness-controlled mold assembled from two polymer plates and a U-shaped silicone spacer. (C) Curing at 65 °C for 30 min. (D) Demolding of the pre-cured PDMS sheet. (E) Formation of the sensing chamber and fluidic ports using manual punches, followed by device assembly.

G. Software and Data System

G.1. Role of the Software in the Sensing System

MatchPD is the mobile software layer of the L-DOPA sensing system. It receives measurement records from the reader, preserves the source current data, derives one analytical result for each sample, and presents longitudinal readings together with medication and daily-context events for overnight review.

The hardware is responsible for electrochemical current generation, digitisation, and wireless transmission. The mobile application begins at the reader interface and is responsible for acquisition management, data integrity, calculation, visualisation, and reporting.

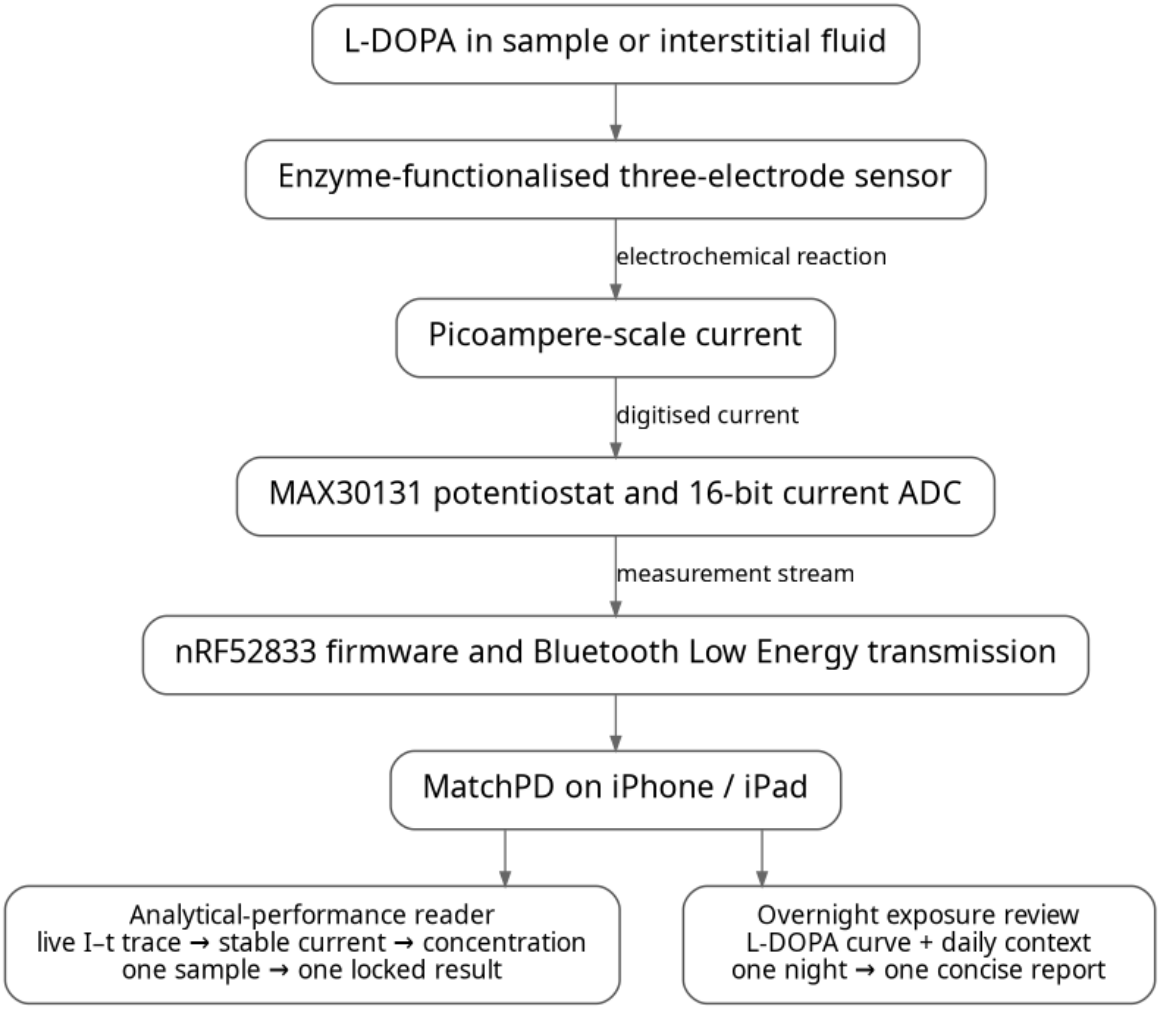


Figure G1. End-to-end data path from electrochemical sensing to mobile readout and longitudinal interpretation.

G.2. Native iOS Architecture and Reader Interface

MatchPD is implemented as a native Swift and SwiftUI application, with Swift Charts used for real-time and longitudinal visualisation. A lightweight feature-based architecture separates device communication, measurement calculation, local records, timeline events, and report presentation.

The Bluetooth layer manages scanning, connection, notification subscription, measurement-session state, and reconnection. Incoming records are decoded once and passed to the measurement store. The application also provides host controls for the measurement configuration, including applied potential, current range, acquisition duration, and start/stop control.

G.3. Analytical-Performance Measurement Workflow

The analytical-performance mode is designed for consecutive flow-cell samples. A measurement session is created for one sample, the application displays the incoming current in real time, and one concentration result is locked at the end of the session.

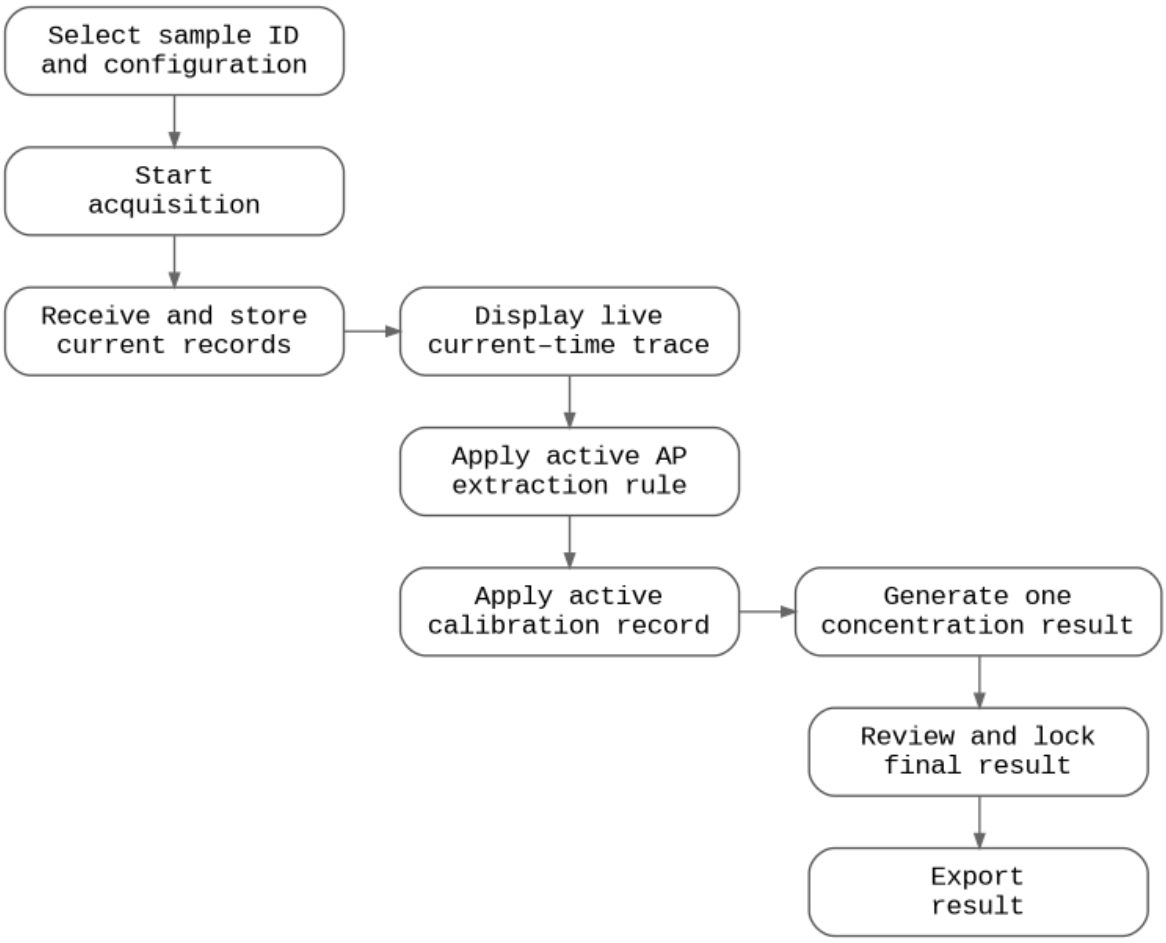


Figure G2. Analytical-performance measurement workflow implemented in MatchPD.

The numerical protocol and calibration relationship used in this mode are those defined for the active analytical-performance electrode in Appendix A. MatchPD applies that protocol to the incoming current stream, stores the calibration identifier together with the result, and preserves the complete source session for inspection and export.

The analytical-performance interface presents the sample ID, measurement status, live current-time trace, calculation region, final concentration, and result-lock state. One sample corresponds to one locked result.

G.4. Longitudinal Monitoring and Contextual Interpretation

The longitudinal mode extends the acquisition pipeline from a single sample to an overnight exposure curve. Sensor readings are placed on one time axis with medication, meal and protein intake, symptoms, sleep, activity, and free-form notes.

The application summarises a night through a small set of directly inspectable features, including onset after medication, whether the signal reaches the patient-specific reference peak, the duration of the elevated interval, and the depth and timing of the overnight nadir. The output is a concise clinician-facing report rather than an automatic treatment decision.



Figure G3. MatchPD longitudinal report integrating L-DOPA readings with medication, sleep, and dietary context.

G.5. Data Integrity, Storage, and Traceability

MatchPD keeps source measurements and derived results as separate records. The raw session contains the reader configuration, sequence numbers, device and phone timestamps, and current values. The derived record contains the extraction rule, calibration identifier, concentration, result state, and export time.

Chart smoothing never overwrites the source values. Missing records remain visible as gaps, retransmitted records are placed by sequence and device time, and a previously locked result is not changed by later notifications. Analytical sessions can be exported as CSV for technical review, while longitudinal summaries are exported as a clinician-readable report.

G.6. User Interface and Application Structure

The application follows a five-tab structure: Home, Log, Guardian, Insights, and Settings. Supporting views provide the unified timeline, doctor report, onboarding, and a dedicated debug surface. The data and interface layers remain independent, so changes to the reader connection or calibration record do not require restructuring the longitudinal timeline or report views.